Numerical and experimental modelling of wave interaction with fixed and floating porous cylinders

Ed Mackay [a],*, Wei Shi [b], Dongsheng Qiao [b], Roman Gabl [c], Thomas Davey [c], Dezhi Ning [b], Lars Johanning [a]

[a] *College of Engineering, Mathematics and Physical Sciences, University of Exeter, UK*
[b] *State Key Laboratory of Coastal and Offshore Engineering, Dalian University of Technology, Dalian, China*
[c] *School of Engineering, Institute for Energy Systems, FloWave Ocean Energy Research Facility, The University of Edinburgh, UK*

ARTICLE INFO

ABSTRACT

We consider wave forces on fixed porous cylinders with and without a solid inner cylinder and wave-induced motions of floating cylinder with and without a porous outer cylinder. Comparisons between experimental measurements and numerical predictions from an iterative boundary element method (BEM) model are presented. The BEM model assumes that pressure drop across porous surface is proportional to the square of the velocity through the surface. It is shown that the BEM model is able to accurately predict the nonlinear variation of the forces with wave amplitude or motion amplitude. It is demonstrated that adding a porous outer cylinder to a solid vertical cylinder leads to increased excitation force on the combined structure. For floating cylinders adding a porous outer cylinder also leads to a corresponding increase in excitation force. However, the porous outer cylinder provides a larger increase in the damping, resulting in reduced motion response. Further numerical simulations indicate that placing the porous cylinder lower in the water column can lead to increased damping without the corresponding increase in excitation forces. It is shown that for low Keulegan Carpenter numbers, the damping coefficient for a porous cylinder is significantly higher than the viscous damping on a solid cylinder. The results suggest that porous materials could be beneficial for motion damping of floating structures.

1. Introduction

Porous materials are often used in marine structures to dissipate wave energy and reduce wave heights around a structure. They have been studied extensively in application to fixed and floating breakwaters (Huang et al., 2011; Dai et al., 2018) and for motion damping of marine structures (Molin and Legras, 1990; Downie et al., 2000a,b; Molin, 2001; Tao and Dray, 2008; An and Faltinsen, 2012, 2013). Porous plates and meshes are sometimes used for absorbing waves in narrow flumes (Evans, 1990; Twu and Lin, 1991; Molin and Fourest, 1992) and to dissipate energy in tuned liquid dampers (Warnitchai and Pinkaew, 1997; Tait et al., 2005; Love and Tait, 2010; Crowley and Porter, 2012; Faltinsen et al., 2011; Molin and Remy, 2013, 2015). The problem of calculating wave interaction with porous structures also arises in for offshore aquaculture (Zhao et al., 2010b).

Given the range of applications of porous materials in offshore engineering, there is a large volume of literature on modelling wave interaction with porous structures. In potential flow models, the porous material is usually modelled as a homogeneous surface where the flow

through the surface is subject to a pressure drop as a function of flow velocity and acceleration. The velocity terms represent dissipation of energy across the porous surface and the acceleration terms represent inertial effects due to the acceleration of the flow through the openings. For thin porous materials, the energy dissipation is proportional to the square of the velocity. However, in many studies the energy dissipation is assumed to be linear in the velocity to simplify the analysis. This approach was taken by Sollitt and Cross (1972) and was further popularised by Chwang (1983) and Yu (1995), who defined a 'porous-effect' parameter, to represent the linearised pressure loss across the porous surface.

The assumption of a linear pressure loss has been adopted in many studies of wave interaction with cylindrical structures. For example, Wang and Ren (1994) used an eigenfunction method to derive analytical expressions for wave loads on a bottom-fixed cylinder surrounded with a porous outer cylinder. Darwiche et al. (1994) studied a similar system, mounted on a cylindrical breakwater. Williams and Li (1998) considered wave interactions with a concentric porous cylinder

mounted on a storage tank. Wave forces on a various types of floating porous cylinder have been derived using an eigenfunction expansion method (Williams et al., 2000; Zhao et al., 2010a; Ning et al., 2017). Wave forces on arrays of porous cylinders have been examined by various authors (Williams and Li, 2000; Li et al., 2004; Sankarbabu et al., 2007; Park et al., 2010; Weng et al., 2016). Short-crested wave interaction with porous cylinders has also been considered in several studies (Song and Tao, 2007; Tao et al., 2009; Liu et al., 2012). The boundary element method (BEM) has also been used to calculate wave loads on porous cylinders (Dokken et al., 2017a; Ouled Housseine et al., 2018; Mackay et al., 2018).

The list above is far from exhaustive, but illustrates the range of studies on porous cylinders which adopt the assumption of linear pressure loss. The limitation of the linear pressure-loss assumption is that the dissipation coefficient must be estimated empirically, with the coefficient depending on the geometry of the particular structure and wave conditions (Li et al., 2006; Suh et al., 2011; Liu and Li, 2016). In particular, the linear model cannot replicate the nonlinear variation of forces with wave amplitude or motion amplitude. Zhao et al. (2010b) conducted experiments with truncated porous cylinders of various porosities and measured excitation forces for the structure held fixed in waves and radiation forces for forced motions. They compared the measurements to predictions from a semi-analytic model using a linear pressure loss law, where the linear dissipation parameter was estimated as a function of wave steepness and porosity, based on the solutions to the diffraction problem. They found that this gave good agreement for excitation forces, but when the same coefficients were used for the radiation problem, the derived added mass and damping coefficients did not agree well with measurements. The reason for this discrepancy is that the linear coefficient is a function of the flow velocity on the structure as well as the porosity. Since the velocity distribution on the structure changes in the radiation and diffraction problems, the same linearised coefficients cannot be used for both cases.

For the case of quadratic pressure loss, various models have been proposed for the pressure loss coefficients that are dependent only on the physical characteristics of the porous surface (porosity, hole spacing, thickness), which are independent of the geometry of the structure and flow velocity (see Molin (2011), Huang et al. (2011) for a review). The quadratic pressure-loss model has been widely applied in studies of two-dimensional (2D) fixed porous barriers (Mei et al., 1974; Bennett et al., 1992; Fugazza and Natale, 1992; Molin and Fourest, 1992; Kriebel, 1992; Liu and Li, 2017; Kim, 1998; Mackay et al., 2019; Mackay and Johanning, 2020; Vijay et al., 2020b,a). It has also been used to examine the added mass and damping properties of porous plates in forced motion (Molin, 2001; Molin et al., 2007; An and Faltinsen, 2012, 2013). Molin (1989) considered the added mass and damping of three-dimensional (3D) porous cylinders in forced motion and assumed they were sufficiently submerged that free surface effects could be ignored. Dokken et al. (2017b) proposed a 3D BEM model with a quadratic pressure loss law, which can solve separately for the radiation and diffraction problems.

A key difference in the case of quadratic pressure loss is that the solutions to the radiation and diffraction problems cannot be superimposed to obtain the solution for body motions in waves, due to the nonlinear pressure–velocity relations on the porous surface. Mackay et al. (2021) proposed a BEM model which solves for the motion response and wave forces on the body simultaneously, under the assumption of quadratic pressure loss. Solutions for the radiation and diffraction problems are obtained as special cases.

The iterative BEM approach for fixed 2D porous structures with quadratic pressure loss has been compared to experimental data in previous studies and shown to give good agreement for the nonlinear variation of forces and reflected waves with wave height (Liu and Li, 2017; Mackay et al., 2019; Vijay et al., 2019). The approach has also been shown to give reasonable predictions for the added mass and

damping coefficients of porous plates and discs under forced heave motions (Molin et al., 2007; An and Faltinsen, 2013). However, there is limited experimental data on wave forces on fixed 3D porous structures or wave-induced motions of floating porous structures.

The motivation for the present study was to investigate the potential of porous materials for reducing loads on fixed offshore structures and reducing wave-induced motions of floating offshore structures. Two simple cases were selected for studying these problems. Firstly, a bottom-fixed porous cylinder, both with and without a solid inner cylinder; and secondly, a similar floating system. The floating system considered was a tension leg platform (TLP) support structure for a floating offshore wind turbine, where the upper column of the TLP was surrounded by a porous outer cylinder (Mackay et al., 2020).

In this work we compare the results of the model tests to numerical predictions from the iterative BEM model described in Mackay et al. (2021). A limitation of the present potential flow approach is that it does not account for viscous effects away from the porous surface. For floating structures with large motion amplitudes, viscous drag forces also become important. To assess the impact of this, we also present some comparisons of the damping on porous cylinders due to energy dissipation across the porous surface with viscous damping on solid cylinders derived in previous studies.

The paper is organised as follows. The mathematical formulation of the problem is described in Section 2 and the experimental setups are described in Section 3. Comparisons of the numerical and experimental results presented in Section 4 for the fixed porous cylinders and Section 5 for the floating porous cylinders (TLP model). Further numerical results for porous cylinders away from the free surface are presented in Section 6. Finally, conclusions are presented in Section 7.

2. Problem formulation

The structure is assumed to consist of a single solid body and a porous surface bounding a volume of water connected to this body. The geometry of the solid body and porous surface are arbitrary and may be either submerged or surface-piercing. A sketch of the setup is shown in Fig. 1, which shows a truncated cylinder with a solid inner column and porous outer surface.

The thickness of the porous barrier and the spacing of the openings are both assumed to be small relative to the incident wavelength, so that the barrier can be treated as a homogeneous surface with a pressure jump across it. The flow through the openings is not modelled explicitly, but approximated using a model for the dissipative and inertial effects as a function of the fluid velocity and acceleration. The effects of the barrier thickness and spacing of the openings are assumed to be captured by the model for the pressure drop across the porous barrier.

The flow through the porous surface is subject to both viscous drag and turbulent dissipation of energy. However, it is assumed that the wakes are quickly homogenised into the flow within a short distance of the porous surface. Away from the porous surface, the fluid is assumed to be inviscid and incompressible, and its motion irrotational, so that a velocity potential can be used to describe the fluid motion. The fluid domain is divided into regions external and internal to the porous boundary, denoted D^E and D^I, with the potentials in the exterior and interior domains denoted Φ^E and Φ^I. The surface of the solid body is divided into two parts, an exterior solid surface, S_E, and an interior solid surface, S_I. The porous surface is denoted S_P. The normal vectors to the body surfaces are defined to point out of the fluid domain on the exterior of the porous surface and into the fluid domain on the interior of the porous surface (see Fig. 1), so that the directions of the normal vectors are continuous over the interior domain. The coordinate system is defined with $z = 0$ on the free surface and $z = -h$ on the sea bed.
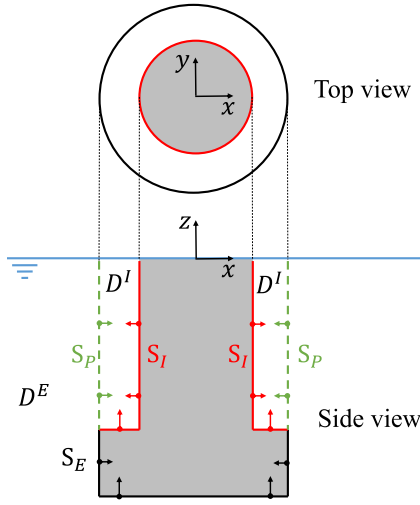
Fig. 1. Sketch of definition of surfaces, normal vectors and internal and external fluid domains.

2.1. Decomposition of potentials

The structure is subject to regular linear waves of amplitude A and angular frequency ω, propagating in a direction at an angle β to the positive x-axis (i.e. $\beta = 0$ corresponds to waves propagating from negative to positive x). The structure is assumed to make 6-DOF harmonic motions of amplitude ξ_j, $j = 1, \dots, 6$, corresponding to surge, sway, heave, roll, pitch and yaw. Under these assumptions the potentials in each domain can be written as

$$\Phi(\mathbf{x}, t)^{E,I} = \text{Re}\left\{ e^{i\omega t} \frac{ig A}{\omega} \phi^{E,I}(\mathbf{x}) \right\}, \tag{1}$$

where g is the acceleration due to gravity, $\mathbf{x} = (x, y, z)$ is the position vector and $\phi^{E,I}(\mathbf{x})$ is the non-dimensional complex amplitude of the potential in each domain. The spatial component is decomposed as

$$\phi^{E,I} = \phi_0 + \phi_7^{E,I} + \sum_{j=1}^{6} \frac{\xi_j}{A} \phi_j^{E,I}, \tag{2}$$

where ϕ_0 is the incident wave potential, $\phi_7^{E,I}$ is the diffracted wave potential and $\phi_j^{E,I}$, $j = 1, \dots, 6$, are the radiated potentials for each mode of motion. Note that ϕ_j is non-dimensional for $j = 1, 2, 3$, but has the dimension of length for $j = 4, 5, 6$. However, the same formulation is used for consistency of notation. The scattered wave potential is defined as the sum of the diffracted and radiated potentials:

$$\phi_s^{E,I} = \phi_7^{E,I} + \sum_{j=1}^{6} \frac{\xi_j}{A} \phi_j^{E,I}. \tag{3}$$

The potentials in each domain satisfy the Laplace equation, the linearised free-surface condition and the no-flow condition on the seabed:

$$\nabla^2 \phi_j^{E,I} = 0, \qquad\qquad j = 0, \dots, 7, \tag{4}$$

$$\frac{\partial \phi_j^{E,I}}{\partial z} = K \phi_j^{E,I}, \qquad z = 0, \quad j = 0, \dots, 7, \tag{5}$$

$$\frac{\partial \phi_j^{E,I}}{\partial z} = 0, \qquad z = -h, \quad j = 0, \dots, 7, \tag{6}$$

where $K = \omega^2/g$ is the infinite-depth wavenumber.

The incident wave potential is given by

$$\phi_0 = e(kz) \exp(-ik(x \cos\beta + y \sin\beta)), \tag{7}$$

where β is the wave direction, k is the finite-depth wavenumber, defined as the positive real solution of $K = k \tanh(kh)$ and the function

$e(kz)$ is defined as

$$e(kz) = \begin{cases} \frac{\cosh(k(z+h))}{\cosh(kh)} & \text{in finite depth,} \\ \exp(kz) & \text{in infinite depth.} \end{cases} \tag{8}$$

The radiated and diffracted potentials in the exterior domain satisfy a radiation condition in the far-field

$$\lim_{R \to \infty} \sqrt{R} \left(\frac{\partial \phi_j^E}{\partial R} + ik\phi_j^E \right) = 0, \quad j = 1, \dots, 7, \tag{9}$$

where $R = \sqrt{x^2 + y^2}$. In the far-field, the radiated and diffracted potentials can be expressed as

$$\lim_{R \to \infty} \phi_j^E = (2\pi kR)^{-1/2} e(kz) \exp(-i(kR + \pi/4)) H_j(\theta), \quad j = 1, \dots, 7, \tag{10}$$

where $\tan(\theta) = y/x$ and $H_j(\theta)$ is the Kochin function, defined as

$$H_j(\theta) = \frac{k}{D(kh)} \int_{S_E \cup S_P} \left(\frac{\partial \phi_j^E(\xi)}{\partial n} - \phi_j^E(\xi) \frac{\partial}{\partial n} \right) \phi_0^*(\xi, \theta) dS, \tag{11}$$

and the star denotes the complex conjugate and the function $D(kh)$ is given by

$$D(kh) = \tanh(kh) + \frac{kh}{\cosh^2 kh}. \tag{12}$$

2.2. Boundary conditions on solid surfaces

The normal vector to the body surface is denoted $\mathbf{n} = (n_1, n_2, n_3)$ and the additional notation $(n_4, n_5, n_6) = \mathbf{x} \times \mathbf{n}$ is adopted. Using this notation, the normal velocity of the boundary of the structure is given by

$$U_n = \text{Re}\left\{ e^{i\omega t} i\omega \sum_{j=1}^{6} \xi_j n_j \right\} = \text{Re}\left\{ e^{i\omega t} i\omega A u_n \right\}, \tag{13}$$

where u_n is a non-dimensionalised velocity of the body surface, defined by

$$u_n = \sum_{j=1}^{6} \frac{\xi_j}{A} n_j. \tag{14}$$

The boundary condition for the scattered potential on the solid surfaces can therefore be written as

$$\frac{1}{K} \frac{\partial \phi_s^{E,I}}{\partial n} = n_s, \quad \text{on} \quad S_E, S_I, \tag{15}$$

where n_s is defined as

$$n_s = n_7 + u_n \tag{16}$$

and

$$n_7 = -\frac{1}{K} \frac{\partial \phi_0}{\partial n}. \tag{17}$$

For fixed structures or for forced motion of a structure in still water, the diffraction and radiation problems can be solved in isolation. In these cases, the boundary conditions for the diffraction and radiation potentials on the solid surfaces are

$$\frac{1}{K} \frac{\partial \phi_j^{E,I}}{\partial n} = n_j, \quad \text{on} \quad S_E, S_I, \quad j = 1, \dots, 7. \tag{18}$$

2.3. Boundary conditions on porous surfaces

The flow through the porous surface in the normal direction is assumed to be continuous on either side of the boundary, so the kinematic boundary condition on the porous surfaces is

$$\frac{\partial \phi_s^E}{\partial n} = \frac{\partial \phi_s^I}{\partial n}, \quad \text{on} \quad S_P. \tag{19}$$

The velocity tangential to the porous surface can be discontinuous on either side. The pressure drop, ΔP, across the porous boundary

is assumed to be the sum of a quadratic drag term due to turbulent dissipation and an inertial term due to acceleration of the flow through the openings:

$$\frac{\Delta P}{\rho} = \frac{1}{2} C_f W_n |W_n| + L \frac{\partial W_n}{\partial t}, \tag{20}$$

where ρ is the fluid density, W_n is the fluid velocity through the porous boundary in the normal direction (assumed to be the average velocity close to the porous boundary rather than the flow speed through the openings), C_f is a dimensionless porous friction coefficient and L is an inertial coefficient with the dimension of length. For the current problems, the porous surfaces are assumed thin, with small hole spacing, so that the representative Keulegan–Carpenter (KC) numbers for the oscillatory flow through the porous barrier are large and the porous friction coefficient C_f can be assumed to take its steady flow values.

The fluid velocity through the porous boundary is the difference between the fluid velocity and boundary velocity, given by

$$W_n = V_n - U_n = \text{Re} \left\{ e^{i\omega t} i\omega A w_n \right\}, \tag{21}$$

where V_n is the velocity of the fluid in the direction normal to the body surface. V_n can be written as

$$V_n = \frac{\partial \Phi}{\partial n} = \text{Re} \left\{ e^{i\omega t} i\omega A v_n \right\}, \tag{22}$$

where v_n is the non-dimensional amplitude of the velocity of the fluid given by

$$v_n = \frac{1}{K} \frac{\partial \phi}{\partial n}. \tag{23}$$

We can therefore write

$$w_n = v_n - u_n. \tag{24}$$

The dynamic pressure is given by the linearised Bernoulli equation as

$$P = -\rho \frac{\partial \Phi}{\partial t}. \tag{25}$$

The time dependence in the quadratic term in (20) can be linearised using Lorenz's principle of equivalent work:

$$W_n |W_n| \approx \frac{8}{3\pi} (\omega A)^2 |w_n| \, \text{Re} \left\{ e^{i\omega t} i w_n \right\}. \tag{26}$$

Substituting (25) and (26) into (20) gives

$$w_n = -i\sigma \left(\phi^E - \phi^I \right), \tag{27}$$

where σ is a non-dimensional quadratic porosity coefficient given by

$$\sigma = \left(\frac{4}{3\pi} C_f K A |w_n| + iKL \right)^{-1}. \tag{28}$$

Eq. (27) can be used to define dynamic boundary conditions on the porous surface for the scattered potential in the combined radiation–diffraction case, the diffraction potential in the fixed case or the radiation potential for the forced motion case. For the scattered potential we have

$$\frac{1}{K} \frac{\partial \phi_s}{\partial n} = n_s - i\sigma \left(\phi_s^E - \phi_s^I \right), \quad \text{on} \quad S_P. \tag{29}$$

In the radiation problem, the same formulation can be used if we assume ξ_j is real and set $A = \xi_j$ and $\phi_0 = \phi_7 = 0$. For both the diffraction and radiation potentials the dynamic boundary condition on the porous surface is

$$\frac{1}{K} \frac{\partial \phi_j}{\partial n} = n_j - i\sigma \left(\phi_j^E - \phi_j^I \right), \quad \text{on} \quad S_P, \quad j = 1, \ldots, 7. \tag{30}$$

2.4. Forces and moments from potential

The total hydrodynamic force (or moment) on the structure in the jth mode, $F_{H,j}$, is the sum of the force (or moment) on the internal and external surfaces

$$F_{H,j} = \rho g A \left[\int_{S_E \cup S_P} \phi^E n_j dS - \int_{S_I \cup S_P} \phi^I n_j dS \right], \quad j = 1, \ldots, 6. \tag{31}$$

Note that the surface normal vectors are pointing in the opposite direction in the interior domain so the integral over the interior surfaces has the opposite sign (see Fig. 1). Similarly, for the diffraction problem, the excitation force (or moment) in the jth mode, F_j, is given by

$$F_j = \rho g A \left[\int_{S_E \cup S_P} \left(\phi_0^E + \phi_7^E \right) n_j dS - \int_{S_I \cup S_P} \left(\phi_0^I + \phi_7^I \right) n_j dS \right], \quad j = 1, \ldots, 6. \tag{32}$$

For the radiation problem, the added mass, a_{ij}, and damping coefficients, b_{ij}, are defined by

$$\omega^2 a_{ij} - i\omega b_{ij} = \rho g \left[\int_{S_E \cup S_P} \phi_j^E n_i dS - \int_{S_I \cup S_P} \phi_j^I n_i dS \right]. \tag{33}$$

The diagonal components of the damping matrix can be expressed in terms of the contributions from wave radiation and energy dissipation across the porous surface (Mackay et al., 2021):

$$b_{jj} = b_{jj}^{rad} + b_{jj}^{por} \tag{34}$$

where

$$b_{jj}^{rad} = \rho \omega \frac{1}{4\pi} \frac{D(kh)}{K^2 k} \int_0^{2\pi} \left| H_j(\theta) \right|^2 d\theta, \tag{35}$$

$$b_{jj}^{por} = \rho \omega \frac{4}{3\pi} C_f \xi_j \int_{S_P} |w_n|^3 dS. \tag{36}$$

2.5. Viscous drag forces

Although the dissipation of energy across the porous surface is a viscous effect, the resulting force is captured by the potential flow model through the parameterised pressure drop model (20). Throughout this paper we use the term 'viscous drag' to refer to forces due to viscous effects which are not captured in the potential flow model. In Section 4 it is shown that the measured forces on the fixed cylinders are in good agreement with the excitation forces from the potential flow model, implying that viscous drag forces are not significant for the range of conditions considered in the experiments. However, the measured motion response of the TLP model for the cases with either no outer cylinder or a solid outer cylinder exhibited a nonlinear variation with wave amplitude around the resonant frequency, implying that viscous drag forces are important in these cases.

In addition to the forces due to the potential flow described in Section 2.4, it is assumed that the surge motion is subject to a drag force due to viscous effects. In this case, for simplicity, the drag force is based on the model surge velocity only, neglecting the velocity of the incident and diffracted waves. Since the drag force is most significant when the RAO is greater than one, this is likely to be a reasonable approximation. The drag force is written as

$$F_d = \frac{1}{2} \rho \mathcal{A} C_d |U_1| U_1, \tag{37}$$

where $U_1 = \text{Re} \left\{ e^{i\omega t} i\omega \xi_1 \right\}$ is the surge velocity and $\mathcal{A}$ is the frontal area of the structure. It is assumed that viscous drag can be treated separately to the forces due to the potential flow, an assumption also adopted in previous studies of porous structures (Molin et al., 2007; An and Faltinsen, 2013). To solve the equation of motion, a linearised drag damping coefficient is defined using Lorenz's principle of equivalent work, defined as

$$b_{11}^{drag} = \frac{4}{3\pi} \rho \omega \mathcal{A} C_d |\xi_1|. \tag{38}$$

The drag coefficient for a solid circular cylinder in oscillatory flow is a function of the Keulegan Carpenter number $KC = |U|T/D$ and the Stokes parameter $\beta = D^2/\nu T$, where $U = \text{Re} \left\{ e^{i\omega t} i\omega \xi \right\}$ is the flow velocity relative to the cylinder, $T = 2\pi/\omega$ is the oscillation period and $D = 2a$ is the diameter of the cylinder. The KC number is the ratio of the displacement of the undisturbed flow to the cylinder radius $KC = \pi \xi/a$. Sumer and Fredsoe (2006) note several distinct flow

regimes depending on the KC number. At low KC numbers the flow is laminar and experimental measurements of C_d (Bearman et al., 1985; Sarpkaya, 1986) have been shown to be in good agreement with the Stokes–Wang model (Stokes, 1851; Wang, 1968):

$$C_d \approx \frac{3\pi^{5/2}}{2\beta^{1/2}KC}. \tag{39}$$

As the KC number increases, instabilities in the flow develop leading to the onset of Honji vortices and an increase in C_d relative to the Stokes–Wang model. As KC increases further, the flow separates and vortices develop, which initially remain attached for intermediate KC numbers and are shed at higher KC. For $\sim 2 < KC <\sim 10$, Graham (1980) found that $C_d \approx 0.2KC$ for circular cylinders. Bearman and Russell (1996) proposed a composite of the Stokes–Wang model for low KC and Graham's model for intermediate KC, given by

$$C_d \approx \frac{3\pi^{5/2}}{2\beta^{1/2}KC} + 0.2KC. \tag{40}$$

There is less information available on drag forces on porous cylinders. The use of porous sheaths has been investigated for reducing vortex shedding and vortex-induced vibration (VIV) from bluff bodies (Rashidi et al., 2016). Durhasan et al. (2019) used particle image velocimetry (PIV) to study the vortex shedding mechanism of a cylinder with a porous outer sheath in steady flow conditions. They found that for the range of conditions investigated, vortex formation in the wake is reduced by the presence of the porous outer sheath. They also found that the drag coefficient of the combined cylinders, referred to the diameter of the outer cylinder, is slightly lower than the drag coefficient of a solid cylinder of the same diameter. Molin (1993) considered a cylinder with a porous sheath in steady flow and estimated the drag force using a potential flow model with a quadratic pressure drop across the porous sheath, similar to that used here. Molin's model did not account for viscous effects away from the porous boundary, so that the drag force would be zero in the limiting cases of the sheath porosity being $\tau = 0$ or 1 (where τ is the ratio of the area of openings to the total area of the sheath). Comparisons with experimental measurements showed that this was a reasonable approximation for a sheath porosity of $\tau = 0.36$, but slightly over-predicts the drag for a porosity of $\tau = 0.2$.

Most previous work on drag forces on porous cylinders has considered the combined effect of drag from the flow through the porous surface and other viscous effects. Moreover, previous studies have considered steady flow. In absence of a model for how drag forces are affected by the presence of the porous outer cylinder in oscillatory flow, for the TLP model we make the simplifying assumption that there is no viscous drag on the porous cylinder and that drag on the solid inner cylinder is unchanged by the addition of the porous outer cylinder. The rationale for this is that, for the range of conditions considered, forces due to flow through the porous cylinder are more significant than other viscous forces. This rationale is explored further in Section 6.1.

2.6. Equation of motion

Due to the high stiffness of the mooring in the heave and pitch directions, the TLP response is modelled as a one degree-of-freedom (DOF) system, with motion restricted to the surge direction. The measurements in the tank confirmed that the pitch motion was minimal and heave was directly coupled to surge, through the motion of the model in an arc about the anchors. The surge–heave coupling is not captured in the linearised frequency domain model. However, since the heave motion is small, the assumption of a single DOF system is reasonable. The equation of motion for the cases with no porous elements can then be written

$$F_1 = \left(C_{m,11} - \omega^2(m + a_{11}) + i\omega(b_{11} + b_{11}^{drag}) \right) \xi_1, \tag{41}$$

where m is the model mass and $C_{m,11}$ is the linearised mooring stiffness in surge. The equation must be solved iteratively due to the dependence

of b_{11}^{drag} on ξ_1. As the radiation and diffraction problems cannot be decoupled for the cases with porous outer cylinders, the equation of motion is written in terms of the total hydrodynamic force as

$$F_{H,1} = \left(C_{m,11} - m\omega^2 + i\omega b_{11}^{drag} \right) \xi_1. \tag{42}$$

Since the total hydrodynamic force is nonlinearly dependent on the body motion, we solve for the motion response and wave forces on the body simultaneously, so that the sum of the radiated and diffracted potentials (i.e. the scattered potential) satisfies the porous boundary condition (29). This is discussed further in the next subsection.

2.7. BEM solution

A BEM solution for the body motions and hydrodynamic forces was presented in Mackay et al. (2021). The resultant system of equations has coefficient matrices containing the porosity coefficient σ, which depends on the normalised fluid velocity through the porous surface w_n. The velocity w_n is the difference between the fluid velocity and the body velocity, both of which are unknown. The system of equations is solved iteratively in two loops, with the fluid velocity calculated in the inner loop based on a first guess for the body velocity. The body velocity is estimated in an outer loop, by finding the motion amplitude ξ_1 which satisfies (42).

3. Experimental setup

Experiments were conducted with two types of model. Various fixed porous cylinders were tested at Dalian University of Technology (DUT). Subsequently, a floating system was tested both at DUT and the FloWave Ocean Energy Research Facility at the University of Edinburgh. The floating system comprised a TLP with a porous outer cylinder. The experimental setup for the fixed porous cylinder tests is described in Section 3.1 and the setup for the floating porous cylinder tests is described in Section 3.2.

3.1. Fixed cylinder models

Tests were conducted with various bottom-fixed vertical circular cylinders, comprising a solid cylinder of outer diameter (OD) 250 mm and five porous cylinders. Three porous cylinders with OD 500 mm were tested with porosities $\tau = 0.1$, 0.2 and 0.3, where the porosity is defined as the ratio of the area of the openings to the total area of porous surface. In addition, two porous cylinders with OD 375 and 750 mm and porosity $\tau = 0.2$ were tested. The perforations in the porous cylinders consisted of circular holes, radius r, arranged in a regular square grid, of side length s, so that the porosity is given by $\tau = \pi r^2/s^2$. In the present tests the square size was fixed at $s = 25$ mm. The thickness of the porous cylinders was 3 mm. The effect of sheet thickness on wave forces was examined in Mackay et al. (2019) and found to have negligible effect in comparison to the porosity.

The water depth at the model location was 1 m. The cylinders all had heights of 1.7 m, with perforations rising to 1.5 m, so that the wave run-up on the structure did not exceed the porous region. Photos of the solid cylinder and one of the porous cylinders are shown in Fig. 2.

Tests were conducted in a wave flume at DUT of length 60 m and width 4 m. A vertical dividing wall of length 13.2 m was installed in the centre of the tank, to create two sections of width 3 m and 1 m. The cylinder models were installed in the wider section and tests with flat porous sheets were conducted simultaneously in the narrower section (see Mackay et al. (2019) for a discussion of the tests with flat sheets). The cylinder models were located in centre of the test section. The models were connected to load cells at top and bottom, to measure horizontal force on the models. A raised section of tank floor was created, so that the lower load cell could be located beneath the raised floor. A schematic showing the layout of the flume, including the dimensions of the raised section of the floor, is shown in Fig. 3.
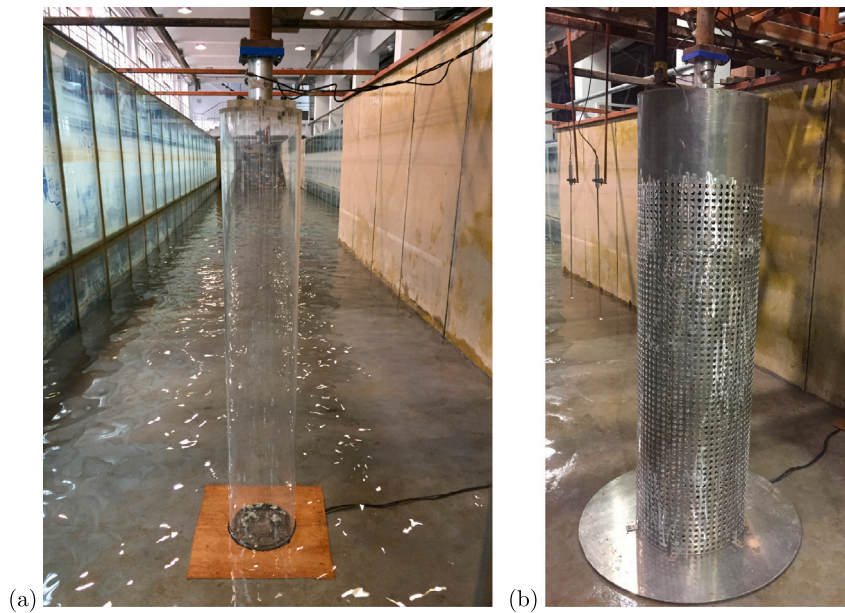
Fig. 2. Photos of fixed cylinder models in the empty tank. (a) Solid cylinder OD 250 mm. (b) Porous cylinder with OD 500 mm and porosity $\tau = 0.3$.
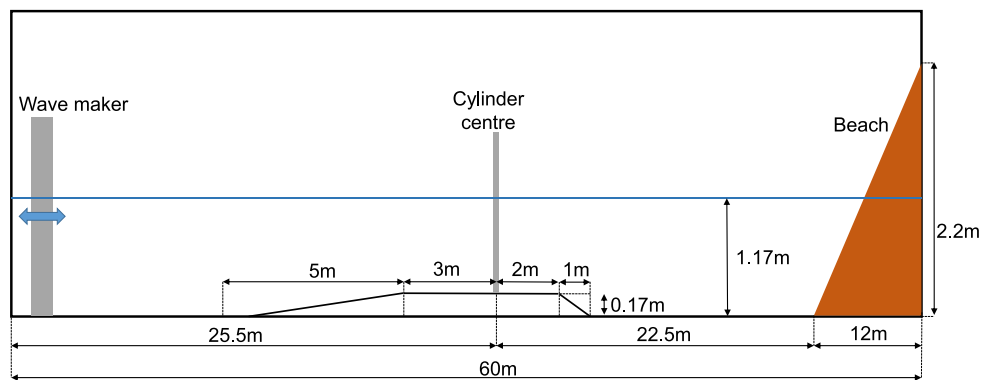

Fig. 3. Schematic of experimental setup in DUT wave flume for fixed cylinder tests (not to scale).

Tests were conducted with various combinations of the solid and porous cylinders, comprising tests with (a) the solid cylinder only, (b) the porous cylinder only, and (c) the solid cylinder inside porous cylinders. In the tests with the solid cylinder inside the porous cylinder, the two cylinders were connected together and the combined force on the inner and outer cylinder was measured. Tests were conducted in regular waves, with $kh \in [0.61, 3.34]$ and $kA \in [0.05, 0.20]$.

3.2. TLP model

The motivation for studying porous materials in the current work was to investigate their use for motion damping of floating wind turbines. A representative 3-leg TLP structure was selected, with dimensions similar to structures tested for the NREL reference turbine design (Koo et al., 2012; Goupee et al., 2014). As the purpose of the tests was to measure the influence of the porous outer cylinders on the hydrodynamic response of the platform, the tests were simplified by not including the aerodynamic or gyroscopic effects of the rotor or the flexibility of the tower, so that the hydrodynamic effects could be examined in isolation. The rotor and nacelle were represented using an equivalent mass at the top of the tower, with the height of the tower and mass of the rotor and nacelle based on the NREL 5 MW turbine design (Jonkman et al., 2009). The dimensions of the model are illustrated in Fig. 4(a) and the mass and volumetric properties are listed

in Table 1. The model was designed to gather data for validation of the numerical method and is not intended to give optimised performance. Both the inner cylinder and porous outer cylinders had a large, vertical freeboard to reduce non-linearities and avoid over-topping. It is also important to note that the model has been intentionally designed to resonate in surge at a frequency which can be excited in the tank, so that the influence of the porous outer cylinders could be measured.

The model was designed to be tested with changeable outer cylinders with various diameters and porosities (see Fig. 4(b)). The outer cylinders used had porosities of $\tau = 0$, 0.15 and 0.3 (where the $\tau = 0$ case is included for reference). The perforations in the porous cylinders were arranged in a square grid, in the same way as for the fixed cylinder tests, with a constant spacing of $s = 25$ mm between hole centres. The outer cylinders had diameters of 222.8 mm and 302.4 mm, giving an integer number of holes around the circumference. The ratios of the diameters of the outer and inner cylinders are approximately 1.6 and 2.2 for the smaller and larger outer cylinders respectively. The wall thickness for the porous cylinders used for the TLP was to 2 mm, reduced from 3 mm used for the fixed porous cylinder tests. The reduction in thickness was required to achieve the correct mass. Mackay et al. (2019) found that the force on fixed porous plates with thicknesses between 3 mm and 10 mm was very similar, so the difference in thickness between the fixed and floating porous cylinders is not expected to have a significant impact on the results.
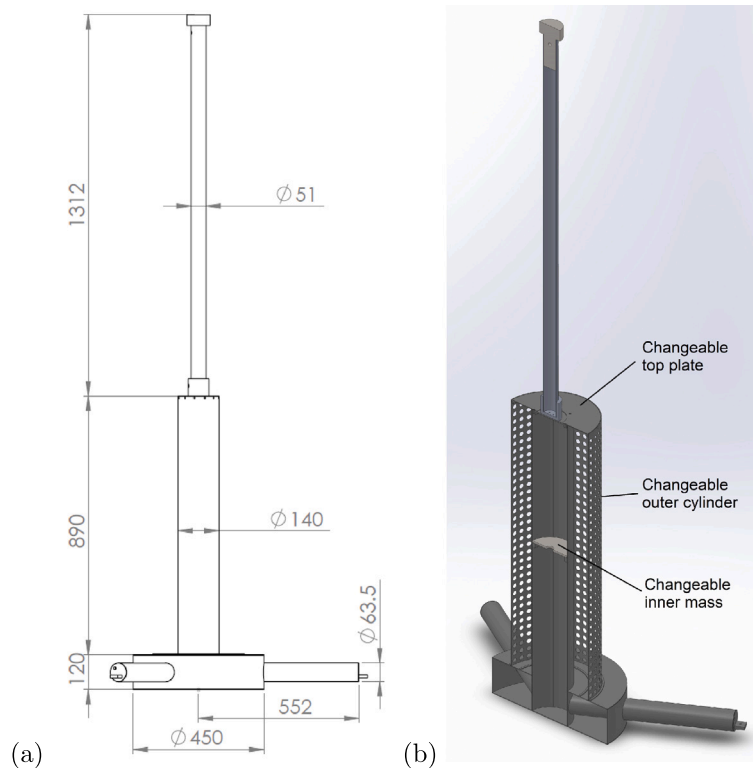
Fig. 4. (a) Dimensions of TLP model (mm) with no outer cylinder. (b) Cross-section of TLP model, including porous outer cylinder.

Table 1
TLP model properties.

Draft [m]	0.60
Displaced volume [m³]	29.6×10^{-3}
Mass [kg]	16.18
Vertical COG [m]	0.222
(relative to MWL, positive upwards)	

To keep the total mass of the model constant between the various configurations, the inner cylinder contained a changeable mass, shown in Fig. 4(b), which could be varied to compensate for the changes in the porosity and diameter of the outer cylinder. The masses were located half way up the column to maintain a constant centre of gravity (COG). The top plate connecting the outer cylinder to the inner cylinder was also changeable, to allow for the different diameters of outer cylinder. The masses of the three top plates (for the configurations with outer cylinders with OD 222 and 302 mm, and the configuration with no outer cylinder) were kept the same. In all seven configurations, the total mass of the model was 16.18 kg and the COG was 222 mm above the still water level. The pitch and roll moments of inertia did vary between model configurations. However, since the moorings had a high axial stiffness, there was very little motion in pitch and roll, with a maximum of less than 1° in the most severe conditions and generally much less than this. The difference in the moments of inertia between configurations is therefore unlikely to influence the comparisons between configurations.

The model was tested both at DUT and FloWave. The same flume used for the fixed cylinder tests at DUT was used, but utilising the full width of the flume, of 4 m and with a constant water depth of 1.2 m along the flume. The mooring comprised three vertical lines of 2 mm diameter Dyneema rope, attached to the ends of the legs and anchored to the tank floor. The locations of the attachment and anchor points are listed in Table 2. The mooring line tension was measured using inline submersible load cells.

The horizontal restoring force for the model is the component of the mooring tension acting in the horizontal direction. The restoring force is nonlinear due to the model moving in an arc and the resultant change in the buoyancy force with the horizontal displacement. The linearised mooring stiffness is $C_{m,11} = T_0/L_0$, where L_0 is the length of the mooring line, $T_0 = \rho V g - mg$ is the pretencion, V is the displaced volume and m is the mass of the model. For the range of conditions considered here, the linearised stiffness results in a good approximation to the measured force (see Mackay et al. (2020) for further details).

The FloWave facility is a circular tank with a diameter of 25 m and a water depth of 2 m, with 168 absorbing wave makers around the circumference. To achieve the same mooring stiffness in the horizontal direction, the mooring was attached to a rigid frame, with the anchor pivot depth equal to that used in the tests at DUT.

For both the tests at DUT and FloWave, the model motions were measured using 6DOF infrared motion capture systems. As the water depth was different at the two sets of tests, we report the measured motions as a function of Ka rather than kh, where $K = \omega^2/g$ is the infinite depth wavenumber and $a = 0.07$ m is the radius of the upper cylinder. The wave frequencies used were in the range $Ka \in [0.01, 0.20]$. In contrast to the tests with the fixed cylinders, the wave amplitude, A, was held constant with frequency, rather than the wave steepness, kA. This was because the main effects of interest for the TLP model occur at low frequencies, so holding kA constant would lead to unrealistically large wave heights at low frequencies. Regular waves with amplitudes $A = 0.02$, 0.04 and 0.06 m were used in both sets of tests.

4. Results for fixed cylinders

The numerical and theoretical results presented in this section assume that the water depth is constant at $h = 1$ m and the influence of the sloped section of the floor is not modelled explicitly. For the BEM calculations for the porous structures we have used Molin and Fourest's model for the porous friction coefficient (Molin and Fourest,
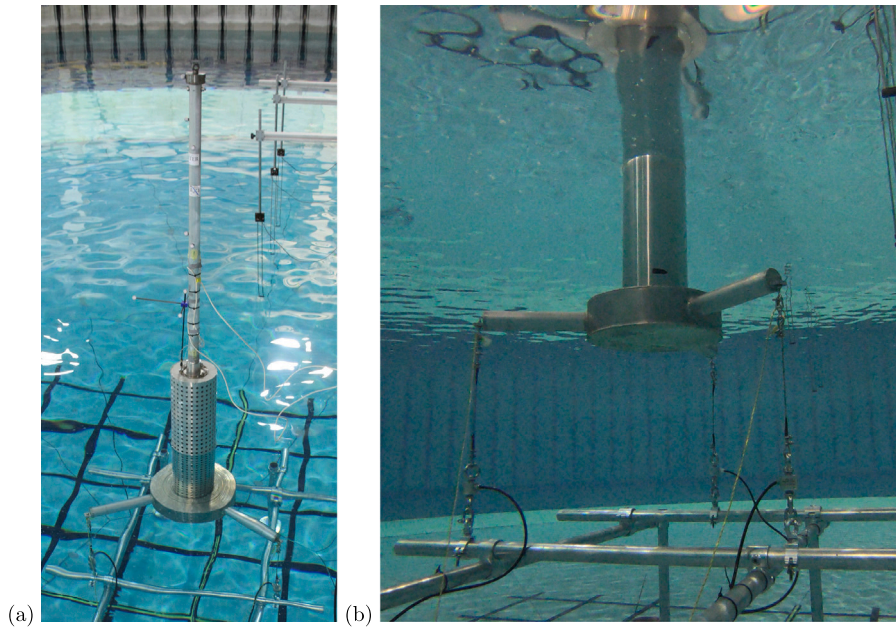
Fig. 5. (a) TLP model with outer cylinder OD 222 mm and porosity $\tau = 0.15$, installed in FloWave tank. (b) Close-up of mooring arrangement and mooring frame in FloWave, configuration shown with solid outer cylinder OD 222 mm.

Table 2
TLP mooring line properties.

Water depth [m]	1.20
Attachment point radius [m]	0.567
Attachment point depth [m]	0.647
Anchor pivot depth [m]	1.158
Mooring line length (pivot–pivot) [m]	0.511
Linearised mooring stiffness in surge [N/m]	258
Water depth for DUT tests [m]	1.2
Water depth for FloWave tests[a] [m]	2.0

[a]Model anchored to raised frame at FloWave—see Fig. 5(b).

1992; Molin, 2011):

$$C_f = \frac{1-\tau}{\mu\tau^2}, \tag{43}$$

where a fixed value of the discharge coefficient $\mu = 0.5$ has been used in this work. The inertial coefficient, L, is modelled using McIver's formulation (McIver, 1998) for the blockage coefficient of a circular hole in a rectangular duct. Reformulating equations (32)–(35) in McIver (1998) gives

$$\frac{L}{s} \approx 0.3898\tau - 0.03239\sqrt{\tau} - 1.2415 + \frac{0.8862}{\sqrt{\tau}}, \tag{44}$$

where s is the hole spacing. This formulation is based on a long-wave assumption, that the thickness of the porous surface is negligible in comparison to the wavelength.

From (28) it is apparent that the ratio of drag to inertial forces on the porous surface is given by

$$\frac{F^{drag}}{F^{inertial}} = \frac{4\,C_f}{3\pi L}\,A\,|w_n|. \tag{45}$$

For the coefficient models used here, the fraction above is fixed for a given value of τ, with $4\,C_f/3\pi L = (1.57, 0.61, 0.36) \times 10^3\,\mathrm{m}^{-1}$ for $\tau = 0.1, 0.2, 0.3$. The relative influence of inertial effects at different wave frequencies is dependent on how A and $|w_n|$ vary with frequency. The variation of $|w_n|$ over the structure and the variation of this with frequency is dependent on the particular structure. However, for the present case, where we have held kA fixed with frequency, we can note that A decreases as k increases, indicating that inertial effects of the porous barrier may be more important at higher frequencies. The wave

amplitudes used in the tests were in the range $A \in [0.015\,\mathrm{m}, 0.154\,\mathrm{m}]$. The magnitude of the normalised velocity through the porous cylinder, $|w_n|$, is $O(1)$, so inertial effects of the porous surface will generally be dominated by drag forces.

Throughout this section we denote the radius of the solid inner cylinder as a and the radius of the porous cylinders as b. The forces are presented in non-dimensional form, normalised by $\rho\,g\,A\,a\,h$. This normalisation is used in all cases, including cases where the solid cylinder is not present, so that the normalisation is consistent when comparing results for porous cylinders with different diameters.

For consistency with the assumptions of the BEM model, the forces measured in the tank tests have been processed to give the equivalent sinusoidal amplitude, given by

$$|F_1| = \sqrt{2\mathrm{Var}(f_1(t))}, \tag{46}$$

where $f_1(t)$ is the measured horizontal force time series and $\mathrm{Var}(.)$ denotes the variance. The section of the time series analysed was defined to be the largest whole number of wave periods, starting after the initial transient response has passed and ending before the reflected waves arrive back from the beach.

4.1. Solid cylinder

Wave forces on solid vertical cylinders have been studied extensively in the past. However, results for the solid cylinder are included here for comparison with the results for the porous cylinders. Under linear wave theory, the normalised horizontal excitation force on a bottom-fixed solid vertical cylinder with circular cross section radius a, is given by MacCamy and Fuchs (1954)

$$\frac{F_1}{\rho g A a h} = \frac{\tanh(kh)}{kh}\frac{4}{ka\,H_1^{(1)'}(ka)}, \tag{47}$$

where $H_1^{(1)}$ is the Hankel function of the first kind of order one and the prime denotes differentiation with respect to the arguments.

Fig. 6 shows the nondimensional measured force amplitude against kh for various values of wave steepness kA, together with the theoretical linear force given by (47). The results generally agree well for the range of conditions shown, and the non-linearity in the measured wave force on the solid cylinder is not evident after processing the
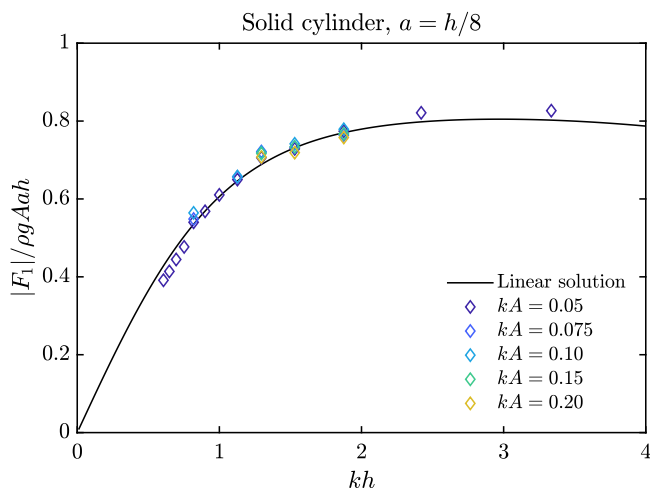
Fig. 6. Nondimensional amplitude of horizontal force on fixed solid cylinder from linear theory (solid line) with measured forces for various wave steepness (diamonds).

measurements in this way. This indicates that the effect of nonlinear components of the potential and viscous drag forces have a small contribution to the total linearised force for the range of conditions considered here. Since the porous cylinders used here have larger diameters than the solid cylinder, the relative contribution of viscous drag will be lower for the porous cylinders. Moreover, as discussed in Section 2.5, drag coefficients are expected to be lower for the porous cylinders. Therefore, neglecting viscous drag forces on the porous cylinders will have a smaller influence than for the solid cylinders.

4.2. Porous cylinders

Fig. 7(a) shows the nondimensional force on the porous cylinder with radius $b = h/4$ against kh for waves with steepness $kA = 0.05$ and for porosities $\tau = 0.1$, 0.2 and 0.3. The results from the BEM model capture the main effects of the cylinder porosity and wave frequency, with good agreement with the measured results in general. The measurements at $kh = 0.82$ and $kh = 1.3$ are somewhat higher than the results from the BEM model, with the discrepancy increasing for the lower porosity cylinders. The measurements for the lower wave frequencies with $kh < 0.8$ are consistently lower than the predictions from the BEM model. These trends are also evident in the results for the solid cylinder, although to a lesser extent (see Fig. 6).

The discrepancies at these frequencies were consistent between tests with various cylinder diameters, porosities and wave steepness, as discussed further below. The effects were also visible in the tests with flat porous sheets, which were conducted simultaneously, as discussed in Mackay et al. (2019). It is suspected that the discrepancies at these frequencies are caused by the interaction of the incident and diffracted waves with the raised section of the tank floor. Although the slope of the front of the raised section is relatively shallow, with a gradient of 3.4%, the entire feature is a similar length to the longer wavelengths used in the tests. The effect of the raised section of the floor was not modelled explicitly in the BEM calculations, so these interaction effects will not be captured. The interaction of the incoming wave with the raised floor will decrease at higher frequencies, as the wave motion decays more rapidly through the water column. This is consistent with the experimental results, which agree better with the numerical results at higher frequencies. It is unclear why the interference is larger for the porous cylinders than the solid cylinders. This will be investigated further in future work. Simulations conducted using a computational fluid dynamics model of the same experimental setup, reported in Qiao et al. (2021), showed excellent agreement with the BEM results. This

gives further weight to the conjecture that the disagreement between the numerical and experimental results is due to uncertainties in the experimental results.

Fig. 7(b) shows the nondimensional force on cylinders with porosity $\tau = 0.2$ against kh for waves with steepness $kA = 0.05$ and for cylinder radii of $b = (3, 4, 6)h/16$. The agreement between the BEM model and experimental measurements is good overall, with the BEM model able to replicate the variation of the force with kh and b/h. The discrepancies at the frequencies mentioned above are also evident in this case.

Fig. 8 shows the nondimensional force on a cylinder with porosity $\tau = 0.2$ and radius $b = h/4$ against kh for various steepness. In contrast to the force on the solid cylinder, discussed in the previous section, there is a significant influence of the wave steepness on the normalised force. At $kh = 1.88$ the normalised force increases from 0.98 for $kA = 0.05$ to 1.91 for $kA = 0.2$. In contrast, at $kh = 1.88$ the measured variation of the normalised force with kA for the solid cylinder is difficult to discern from the experimental uncertainty. The BEM model accurately replicates the effect of the wave steepness on the normalised force on the porous cylinder (notwithstanding the effects of the raised floor, discussed above), indicating that the quadratic pressure drop model accurately captures the large-scale effects of the porous surface on the flow.

From (28) it can be seen that for a given frequency, a change in the wave amplitude has the same effect on the normalised force as a change in the porous friction coefficient C_f. This is evident from the similarity between Figs. 7(a) and 8, which display similar effects of changes in kA and τ. However, it should be noted that the nonlinear relationship between τ and C_f mean that changes in τ have a proportionally larger effect than changes in kA for the values shown here.

4.3. Porous cylinder with solid inner cylinder

Fig. 9(a) shows the combined nondimensional force on porous cylinders with a solid inner cylinder for a ratio of outer to inner radius of $b/a = 2$ and inner radius $a = h/8$, plotted against kh for waves with steepness $kA = 0.05$ and for outer cylinder porosities $\tau = 0.1$, 0.2, 0.3 and 1. The case with $\tau = 1$ corresponds to the case with no outer cylinder, and is included here for reference. In comparison to the cases with no inner cylinder, shown in Fig. 7, the presence of the inner cylinder causes a small reduction in the peak value of $|F_1|$. The inner cylinder also results in an increase in the value of $|F_1|$ at higher frequencies.

Compared to the case with the inner cylinder only, adding a porous outer cylinder significantly increases the load on the combined structure at lower frequencies. At higher frequencies the outer cylinder has a smaller effect. The BEM model results generally agree well with the measurements, although there is a small but consistent underestimation of the force at higher frequencies which did not occur for the cases with no inner cylinder.

Fig. 9(b) shows the effect of the outer cylinder diameter for fixed porosity and wave steepness. The case with $b/a = 1$ corresponds to the case with no outer cylinder. The BEM model is able to capture the variation of the force with the outer cylinder diameter in this case as well.

5. Results for floating cylinders

The experiments at DUT used 13 wave frequencies and 3 wave amplitudes and covered configurations with both outer cylinder diameters. The tests at FloWave used 26 wave frequencies, but only 2 wave amplitudes and only covered configurations with the smaller outer cylinder. The experimental results have been analysed in a similar way to the results for the fixed cylinders. The motion and wave amplitudes are defined as

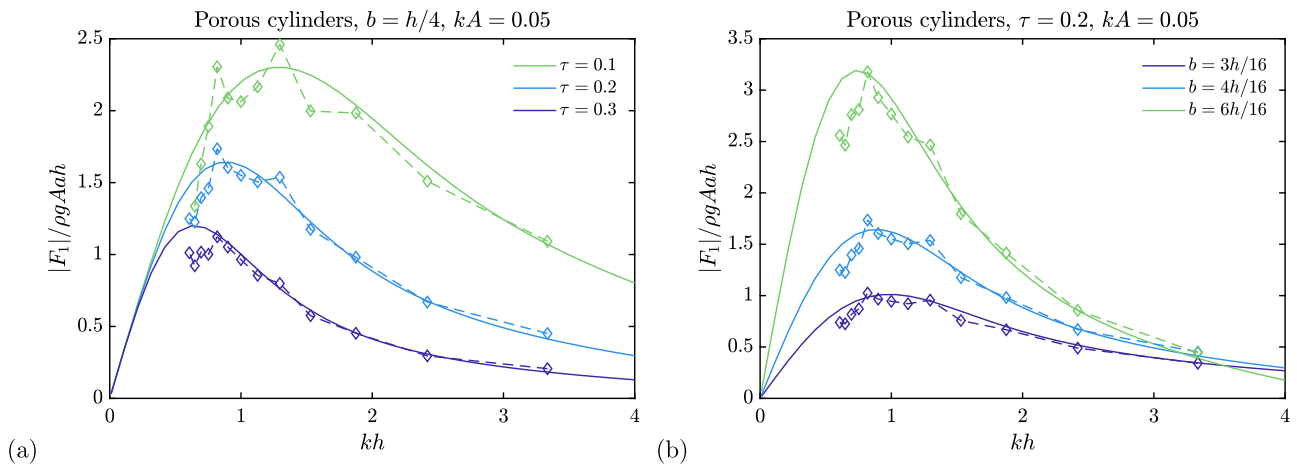$$\xi_1 = \sqrt{2 \operatorname{Var}(x(t))}, \tag{48}$$

Fig. 7. Nondimensional amplitude of horizontal force on fixed porous cylinder from BEM model (solid line) and measurements (diamonds). (a) For various cylinder porosities. (b) For cylinders of various radii.
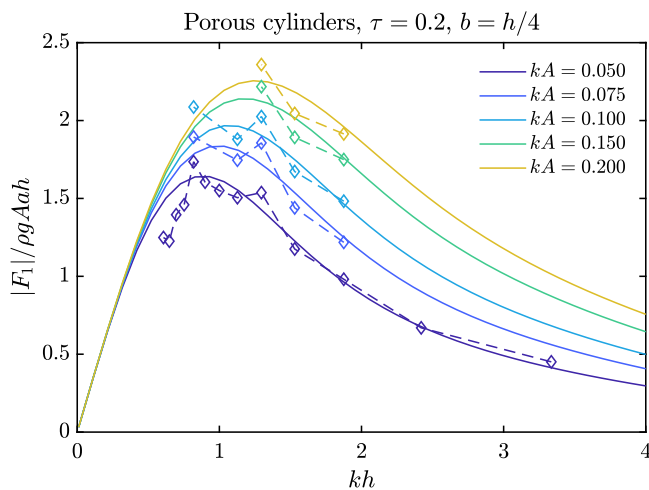

Fig. 8. Nondimensional amplitude of horizontal force on fixed porous cylinder from BEM model (solid line) and measurements (diamonds) for various wave steepness.

$$A = \sqrt{2\,\mathrm{Var}(\eta(t))}, \tag{49}$$

where $x(t)$ is the surge motion time series and $\eta(t)$ is the surface elevation time series, measured in the empty tank. In contrast to the tests with fixed cylinders, the portion of the record analysed is the quasi-steady state period, after the reflected waves had arrived back from the beach. This is because in several cases, the initial transient effect did not decay until after the reflected waves had arrived at the model location. An analysis of the reflected waves for both sets of tests is presented in Section 5.1.

As the focus of the present work is to examine the influence of the porous outer cylinder on the motion response of a structure, the drag coefficients for the solid structures are estimated empirically from the experiments, as described in Section 5.2. Due to the complex shape of the TLP, we make the simplifying assumption that the drag coefficient is constant, with no dependence on the Keulegan–Carpenter (KC) number.

Although the excitation and radiation forces were not measured in the tank, it is instructive to examine the numerical predictions of these forces in order to explain the influence of the porous outer cylinder on the model motions. Numerical predictions of radiation and diffraction forces are discussed in Section 5.3. This also allows us to assess the relative importance of damping due to wave radiation, dissipation of energy across the porous surface and viscous drag.

Throughout the section, results are presented in terms of the surge response amplitude operator (RAO), defined as $|\xi_1|/A$. In contrast to the results for fixed cylinders, results are plotted as a function of Ka, where $a = 0.07\,\mathrm{m}$ is the radius of the upper cylinder of the model. This variable is used on the abscissa rather than kh, since the water depth differed in the two sets of tests. The variable b is used to denote the radius of the outer cylinder. The effects of the porosity of the outer cylinder and the wave amplitude are discussed in Sections 5.4 and 5.5.

5.1. Analysis of reflected waves

For both sets of tests, waves were measured in the empty tank and reflections were estimated using the three-probe least squares method (Mansard and Funke, 1980). The reflection coefficients, C_r, for the DUT flume and FloWave tank are shown in Fig. 10. The DUT flume has a large reflection coefficient at lower frequencies of up to 0.4, but a lower reflection at higher frequencies, since the beach is more efficient for short wavelengths. In contrast, the reflection coefficient at FloWave is relatively constant with frequency, with $C_r \approx 10\%$. Given the different reflection characteristics, the data from the DUT tests is expected to be more reliable at high frequencies, and the data from FloWave is expected to be more reliable at low frequencies.

5.2. Estimation of drag coefficients

The drag coefficient was estimated to give the best agreement between the BEM model and the experimental results for tests with either no outer cylinder or solid outer cylinders. For these cases the numerical model used was a standard single-domain BEM model for solid bodies, with no inner volume of water. This means that the results for the cases with solid outer cylinder make the tacit assumption that the entrained water between the inner and outer columns behaves like a solid mass. This will not capture any sloshing effects of the internal water. However, a comparison between the numerical and experimental results indicated that this was a reasonable approximation for the range of conditions considered.

Fig. 11 shows the surge RAOs for the tests with no outer cylinder and tests with solid outer cylinders for various wave amplitudes. The BEM results were calculated using a drag coefficient of $C_d = 1.2$. The agreement is reasonable for the range of conditions shown. For the tests in a water depth of 1.2 m, there is an increased response at low frequency in the experimental data which is not present in the numerical predictions. It is suspected that this is due to uncertainties caused by the increased wave reflections at low frequencies. The absence of this effect in the measurements at the FloWave facility support this
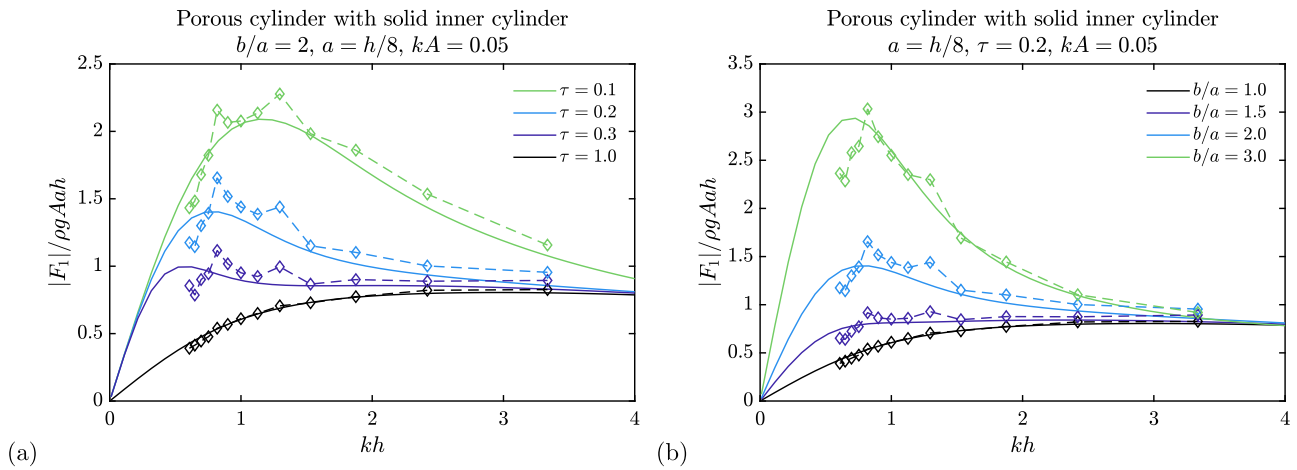
Fig. 9. Nondimensional amplitude of horizontal force on fixed porous cylinder with solid inner cylinder from BEM model (solid line) and measurements (diamonds). (a) For outer cylinders of various porosities. (b) For outer cylinders of various radii.
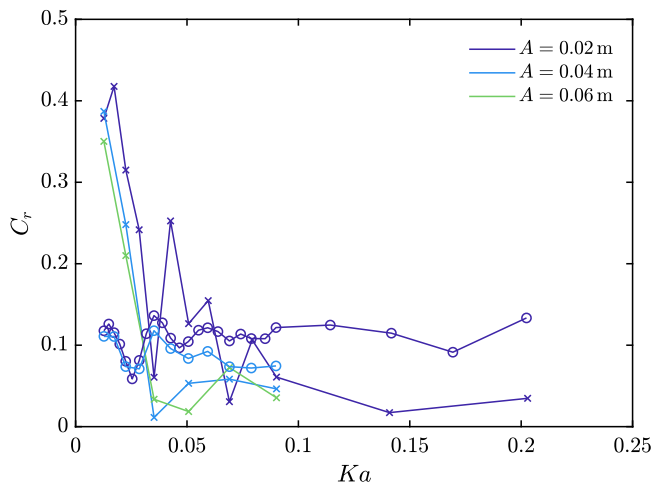

Fig. 10. Estimated reflection coefficients from regular wave tests in DUT (crosses) and FloWave (circles) for various wave amplitudes.

hypothesis, as the reflections at low frequencies were lower in this case. The RAOs estimated from the FloWave tests exhibit an oscillation with Ka, similar to the effect observed in the measured wave conditions discussed in the previous section. This effect is therefore expected to be a result of the reflections in the tank. Note that for $Ka > 0.1$, the frequency spacing of the regular wave tests was relatively coarse, so the oscillatory behaviour of the RAO is not evident. In other tests in irregular waves (not reported here), the oscillatory behaviour at high frequencies was visible.

Aside from the effects discussed above, the frequency response and amplitude is well-replicated by the numerical predictions. The non-linearity in the mooring is small over range of motion considered (see Mackay et al. (2020) for details). The use of the constant drag coefficient is reasonably effective at replicating the measured RAOs for the various outer cylinder diameters, wave conditions and water depths.

5.3. Diffraction and radiation forces

Fig. 12 shows numerical predictions of the surge excitation force, added mass and damping on the TLP model for the case with outer cylinder radius $b = 0.111$ m and water depth $h = 1.2$ m and various outer cylinder porosities. The cases with a solid outer cylinder ($\tau = 0$) and no

outer cylinder ($\tau = 1$) are also included for comparison. Note that the diffraction and radiation problems have been solved separately using a wave amplitude of $A = 0.02$ m and motion amplitude $\xi_1 = 0.02$ m respectively. From (28) it is apparent that a change in either the wave or motion amplitude has the same as effect on the normalised forces as a change in the porous friction coefficient C_f, so the results for different cylinder porosities give an indication of how the diffraction and radiation forces change with wave and motion amplitudes. The excitation forces, added mass and damping coefficient are shown in nondimensional form, with $d = 0.6$ m denoting the model draft and $V = 26.9 \times 10^{-3}$ m³ denoting the model volume.

As the porosity of the outer cylinder tends to zero, the surge excitation force tends towards the value for the case with a solid outer cylinder. Conversely, as the porosity of the outer cylinder increases, the excitation force tends towards the value for the case with a no outer cylinder. For $\tau = 0.3$, the excitation force is very close to the case with no outer cylinder.

For the case with a solid outer cylinder, the mass of water entrained between the inner and outer cylinders has been added to the added mass calculated by the BEM model. This adjustment has been made for consistency with the results for the cases with porous outer cylinders, which already account for the effect of the entrained mass of water. After this adjustment, it is evident that the effect of changing the porosity of the outer cylinder is to move between the cases with a solid outer cylinder and no outer cylinder. For the present case, there is very little change in the added mass for an outer cylinder porosity of $\tau = 0.3$.

The wave radiation damping and porous damping are shown in Figs. 12(c) and (d) respectively. Note that for the cases with no outer cylinder and solid outer cylinders, the porous damping is zero. The wave radiation damping is relatively low for the range of Ka considered, tending to zero as $Ka \to 0$. As with the excitation force and added mass, the wave radiation damping for an outer cylinder porosity of $\tau = 0.3$ is very close to the value for no outer cylinder. In contrast, the porous damping is significantly higher than the radiation damping and the normalised value is relatively constant with frequency. The porous damping initially increases as the porosity increases from zero, then decreases again, with the case with $\tau = 0.1$ leading to the highest values of b_{11}^{por}. In contrast to the other variables considered, there is still a significant influence of the outer cylinder with a porosity of $\tau = 0.3$.

From Eqs. (36) and (38), the ratio of damping from flow through porous surface to viscous drag damping is given by

$$\frac{b_{11}^{por}}{b_{11}^{drag}} = \frac{C_f}{C_d} \frac{\int_{S_P} |w_n|^3 \, dS}{\mathcal{A}}. \tag{50}$$
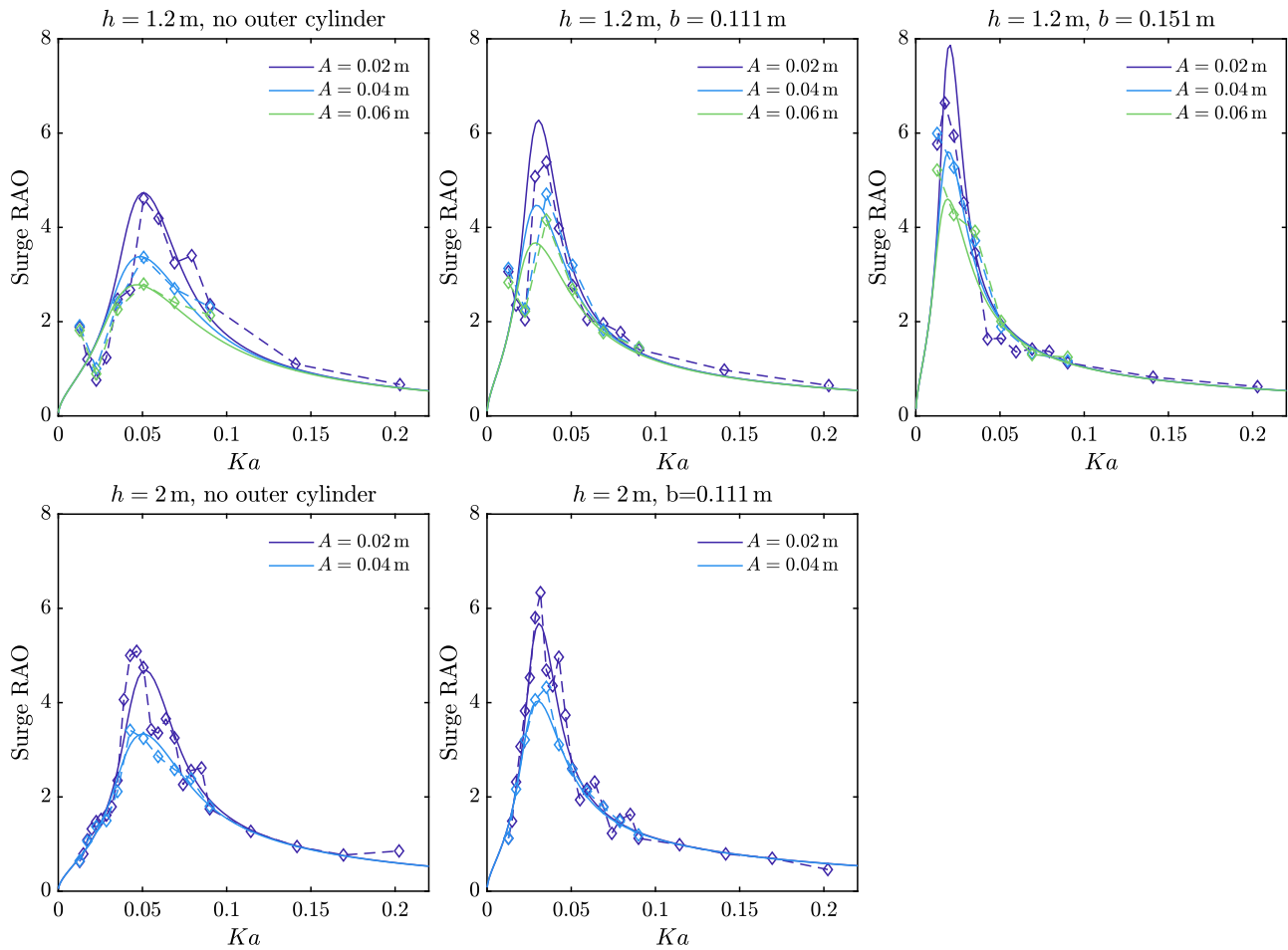
Fig. 11. Surge RAOs for configurations with no outer cylinder or solid outer cylinders, against Ka for various wave amplitudes, from BEM model (solid lines) and measurements (diamonds). Upper row: Tests in water depth $h = 1.2$ m. Lower row: Tests in water depth $h = 2$ m.

In the present case, the frontal area of the model is taken as $\mathcal{A} = 0.157$ m^2 and the drag coefficient for the cases with no porous elements was estimated at $C_d = 1.2$ and was assumed constant with both frequency and amplitude. The porous friction coefficient C_f is also assumed to be independent of flow conditions, which was shown to be a reasonable approximation for the case of fixed cylinders. The relative importance of viscous drag therefore depends on how the integral of $|w_n|^3$ varies with frequency. From Fig. 12(d) it is apparent that the integral of $|w_n|^3$ is approximately constant with frequency. The value of C_d is likely to be reduced for the porous cylinders. However, taking $C_d = 1.2$ as an upper bound, gives the ratio $b_{11}^{por}/b_{11}^{drag}$ in the range 2.5 – 7.5 for the configurations considered here. Since the porous damping is several times larger than the viscous damping, the errors resulting from the assumption that viscous drag on the inner cylinder is unchanged by the presence of the porous outer cylinder are likely to be relatively small.

5.4. Effect of porous outer cylinders on motion response

Fig. 13 shows the effect of the porosity of the outer cylinder on the motion response for tests in both water depths and with both outer cylinder diameters. The results for $\tau = 1$ correspond to the case with no outer cylinder and the results for $\tau = 0$ correspond to the case of a solid outer cylinder. The oscillatory behaviour in the experimental results from FloWave are evident here as well. The frequencies of the oscillations are consistent between the tests with different configurations, with and without outer cylinders. This indicates that this is not a result of any fluid sloshing effects between the inner and outer cylinder,

or an effect of the porous wall. The oscillatory behaviour is not present in the BEM results for any case. Since the case with no outer cylinder is a standard floating solid body problem, we would expect results from linear hydrodynamic models to give reasonable results in this case. The absence of the oscillatory behaviour in the BEM results therefore suggests that the oscillatory behaviour is due to the effect of reflected waves, present in the FloWave tank.

The inclusion of the solid outer cylinder shifts the resonant response to a lower frequency due to the increase in added mass (including the mass of entrained water between the inner and outer cylinders). The peak response amplitude is also increased due to the reduced radiation damping at lower frequencies. The larger diameter outer cylinder causes a larger shift in the resonant frequency due to the larger change in mass. The effect of the outer cylinders is similar in both water depths.

Increasing the porosity of the outer cylinder from $\tau = 0$ to $\tau = 0.3$ leads to an increase in the frequency of the peak response and a reduction in its amplitude. This is due to a reduction in the added mass and increase in the damping, discussed in the previous section. The peak response increases when the porosity is increased from $\tau = 0.3$ to $\tau = 1$ (no outer cylinder). The porosity which leads to the lowest peak response will, in general, be case-specific.

There is a reasonable qualitative agreement between the experimental and numerical results. However, due to the effect of reflected waves on the experimental results mean, there is some uncertainty in the frequency and amplitude of the peak response. Nevertheless, the BEM model is able to predict the main effects measured in the tank.
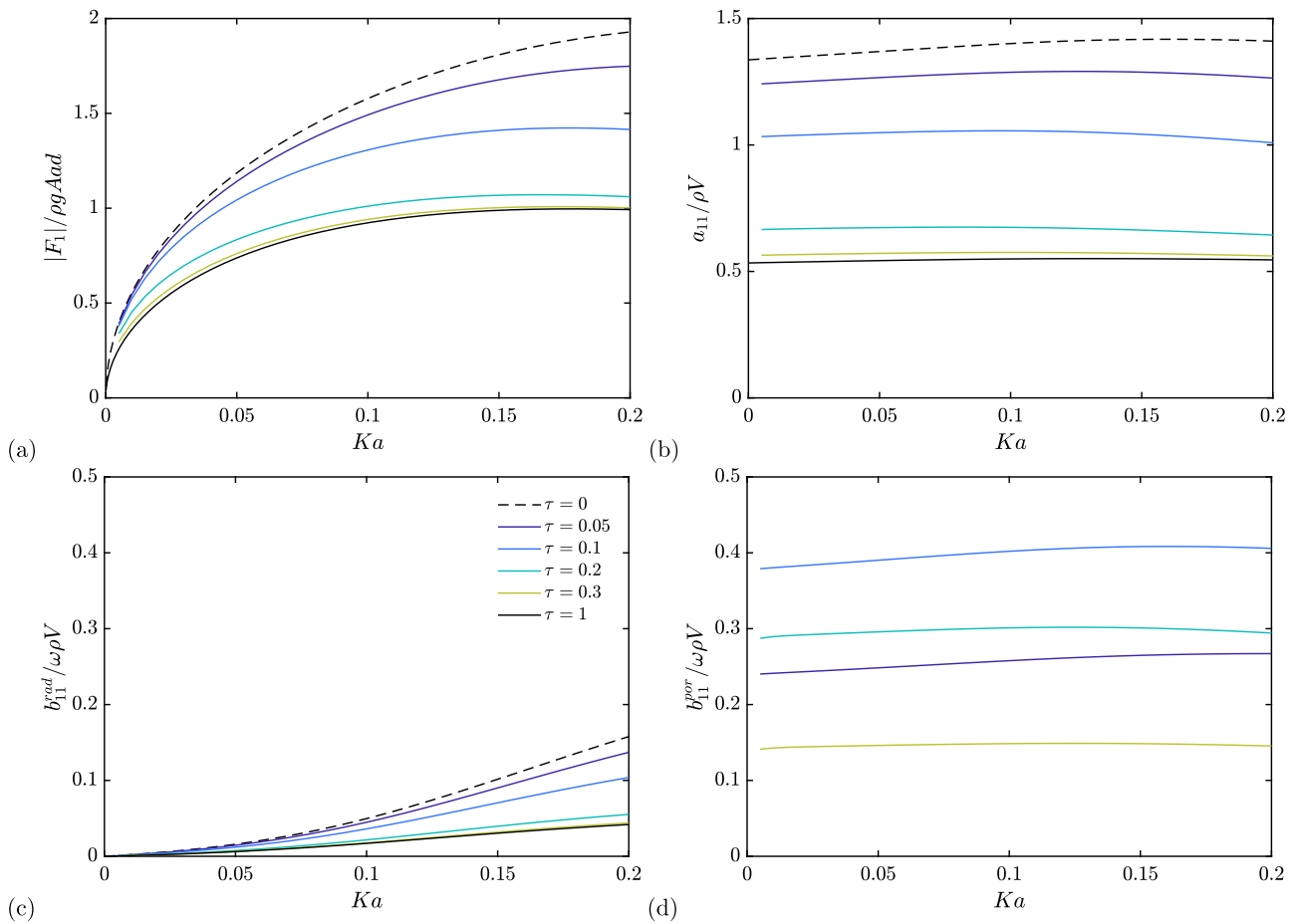
Fig. 12. Numerical predictions for the TLP model of (a) surge excitation force, (b) surge added mass, (c) surge radiation damping, and (d) surge porous damping. Results for case with outer cylinder radius $b = 0.111$ m, wave amplitude $A = 0.02$ m, motion amplitude $\xi_1 = 0.02$ m, and water depth $h = 1.2$ m.

5.5. Effect of wave amplitude on motion response

Fig. 14 shows the RAO from the BEM model and experiments for the tests in water depth $h = 1.2$ m with outer cylinder radius $b = 0.111$ m and porosity $\tau = 0.15$. The results are qualitatively similar, with the BEM model predicting a similar magnitude of effect, both around the peak and at higher frequencies. However, due to the uncertainties in the measurements due to wave reflections, there are differences between the measured and predicted response at low frequencies. As the effect of increasing the wave amplitude is the same as increasing the porous friction coefficient, C_f, the response at higher frequencies is reduced in higher wave amplitudes, and there is a small increase in the response at lower frequencies, due to the increase in added mass.

6. Further numerical results

The motivation for the present study was to investigate the use of porous materials reduce either wave-induced loads or motions for offshore structures. The results for both the fixed and floating cylinders show that adding a porous outer cylinder increases the excitation forces on the structure. However, the results for the TLP model indicated that the increase in damping resulted in reduced motions, despite the increased excitation force. It is therefore interesting to examine whether the damping could be increased without an increase in the excitation force, if the porous elements are placed lower in the water column.

A limitation of the current numerical approach is that it does not account for viscous effects away from the porous surface. To examine how the porous damping compares to viscous damping on a solid

cylinder, we first consider the forces on a 2D porous cylinder in an oscillatory flow.

6.1. Force on a 2D porous cylinder

Consider an infinitely long porous cylinder, with circular cross section, radius a. We consider a 2D cross-section of the cylinder in a harmonically oscillating flow in the x-direction, with angular frequency ω and amplitude ξ. We follow a similar approach to that described in Section 2 and estimate the force on the cylinder using a potential flow approach, with the dissipation across the porous wall of the cylinder represented by the pressure drop model (20). In the present study, as above, we assume inertial effects of flow through the porous wall are negligible and set $L = 0$. The same approach was taken by Molin (1993) to estimate the drag force on a solid cylinder surrounded by a porous sheath in steady flow. The use of a potential flow approach means that the drag force will be zero when the porosity is zero (d'Alembert's paradox). The method is justified on pragmatic grounds, under the assumption that for moderate porosities and low KC numbers, drag from flow through the porous cylinder will dominate over drag from viscous effects away from the porous cylinder wall.

As before, we consider the potential in the domains exterior and interior to the porous cylinder and write the time-dependent potential in polar coordinates as

$$\Phi^{E,I}(r, \theta, t) = \text{Re}\left\{ \omega \xi a \psi(r, \theta)^{E,I} e^{i\omega t} \right\}, \tag{51}$$
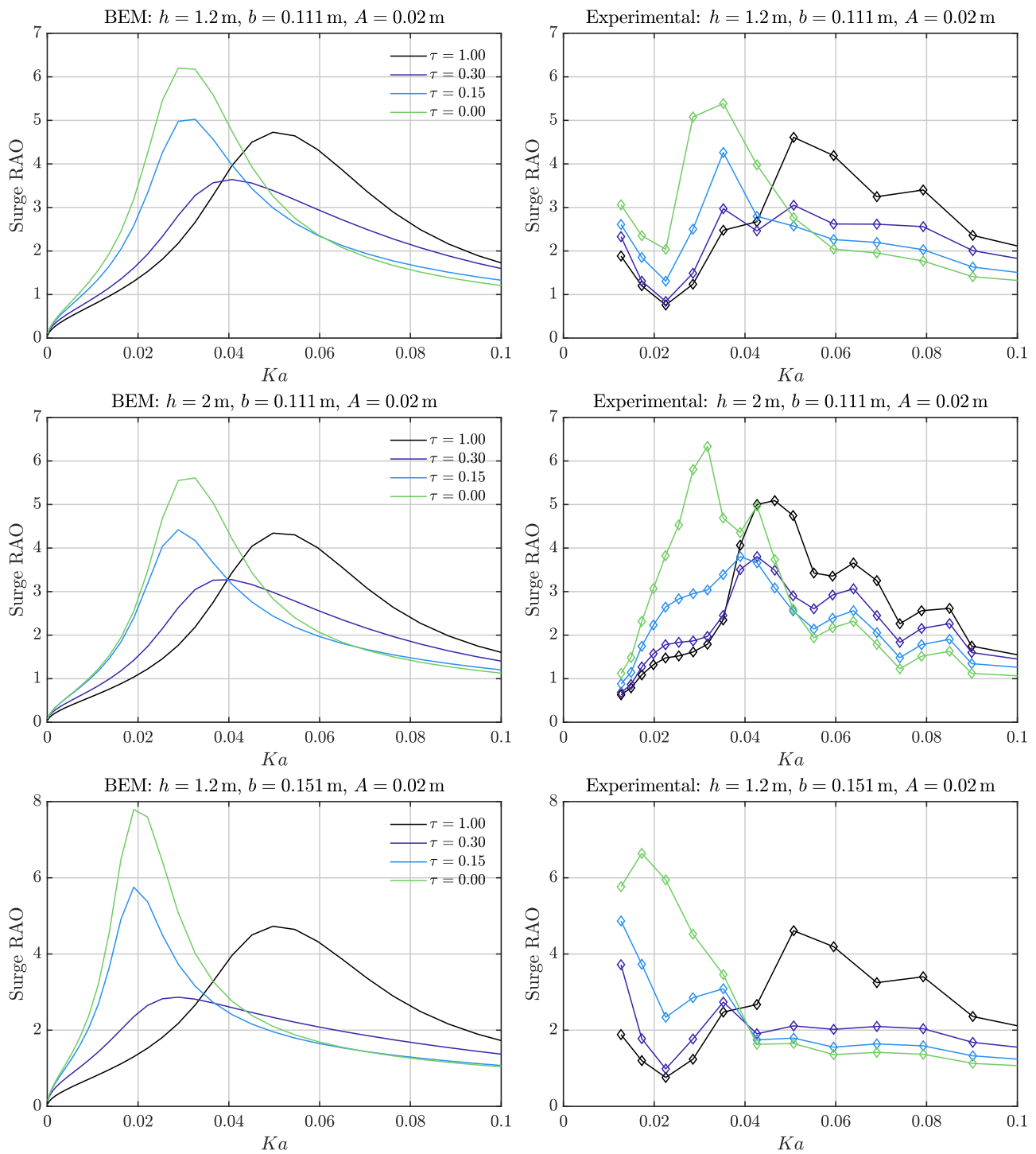
Fig. 13. Effect of outer cylinder porosity on surge RAOs for wave amplitude $A = 0.02$ m and various combinations of water depth and outer cylinder radius. Left: BEM results. Right: Experimental results.

where $\psi^{E,I}(r,\theta)$ is the non-dimensional spatial component of the potential, given by

$$\psi^{E,I} = \frac{r}{a}\cos(\theta) + \phi^{E,I}. \tag{52}$$

It is assumed that the amplitude of the flow is small, so that the velocity-squared terms in the Bernoulli equation can be neglected and the dynamic pressure is given by (25). After a similar analysis to that in Section 2.3, the dynamic boundary condition on the porous surface

can be written

$$\frac{4}{3\pi}C_f\frac{\xi}{a}|w_n|w_n = -i(\phi^E - \phi^I), \tag{53}$$

where w_n is the non-dimensional normal velocity through the porous boundary given by

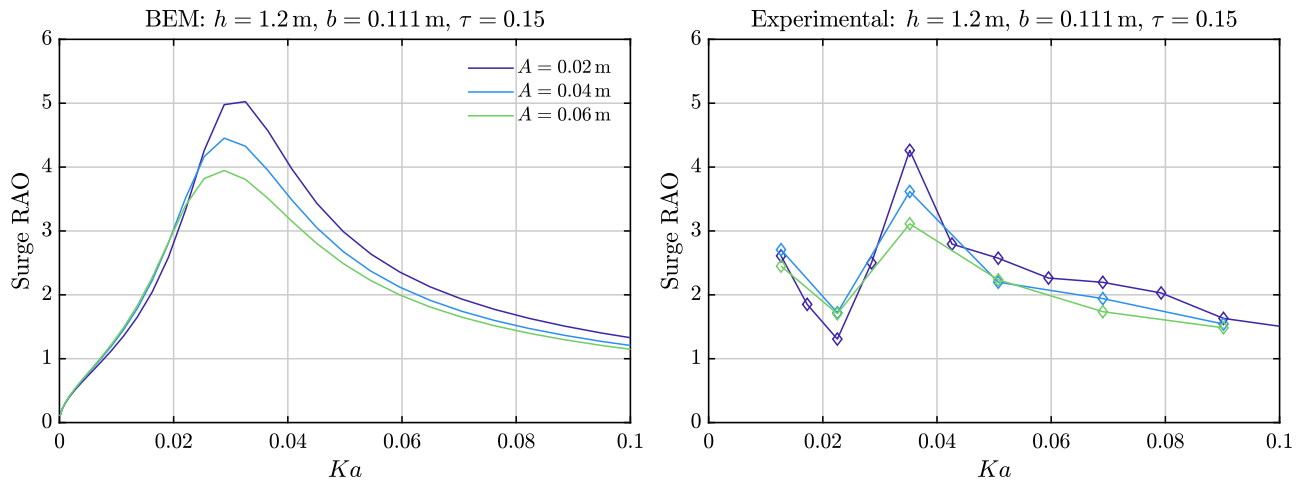$$w_n = \cos(\theta) + a\frac{\partial\phi^{E,I}}{\partial r}. \tag{54}$$

Fig. 14. Effect of wave amplitude on surge RAOs for $h = 1.2\,\text{m}$ and outer cylinder with radius $b = 0.111\,\text{m}$ and $\tau = 0.15$. Left: BEM results. Right: Experimental results.

The non-dimensional complex amplitude of the force per unit length, d, is given by

$$f = \frac{F_1}{\rho \omega^2 \xi \pi a^2 d} = \frac{i}{\pi} \int_0^{2\pi} (\phi^E - \phi^I) \cos(\theta) d\theta$$

$$= -\frac{4}{3\pi^2} C_f \frac{\xi}{a} \int_0^{2\pi} |w_n| w_n \cos(\theta) d\theta. \tag{55}$$

The normalised added mass and damping coefficients per unit length are therefore:

$$\frac{a_{11}}{\rho \pi a^2 d} = \text{Re}\{f\}, \tag{56}$$

$$\frac{b_{11}}{\omega \rho \pi a^2 d} = \text{Im}\{f\}. \tag{57}$$

The coupled system of equations for ϕ^E and ϕ^I has been solved using an iterative BEM model, similar to that described in Mackay and Johanning (2020), Mackay et al. (2021). Molin (1989, 2011) also considered the same problem, but applied an additional linearisation of the angular variation of the potential around the cylinder, and used this to derive analytical expressions for the added mass and damping coefficients. The analytical expressions differ slightly from the solutions from the BEM model, giving lower added mass and a higher peak damping. The solution from the BEM model is considered more accurate as it does not require linearisation of the angular variation of the potential.

Under the current assumptions, the forces on the cylinder are governed by the dynamic boundary condition (53), which depends only on the porous friction coefficient C_f and the amplitude to radius ratio ξ/a, or equivalently the KC number, but is independent of the frequency. Therefore, for the present model, the added mass and damping coefficients are dependent on C_f and KC only.

Figs. 15(a) and (b) show the normalised added mass and damping coefficients as a function of the porosity τ, for $KC = 1$, 2, 4 and 8. The porous friction coefficient C_f has been calculated using (43) with $\mu = 0.5$. The added mass coefficient decreases monotonically with increasing porosity, from a value of 2 for a solid cylinder, to zero when the porosity is one (i.e. no cylinder). The effect of increasing KC is equivalent to increasing C_f, i.e. the porous cylinder behaves more like a solid cylinder as the oscillation amplitude increases.

In contrast, the damping coefficient is zero for the case of a solid cylinder, due to the assumption of inviscid flow. The damping coefficient increases to a maximum of around 0.9, then decreases back towards zero as the porosity approaches one. The value of porosity that gives the maximum damping is dependent on the KC number, with the porosity that gives the maximum damping increasing with the KC number.

Figs. 15(c) and (d) show the added mass and damping coefficients as a function of KC number for various porosities. Both the added mass and damping tend to zero as KC tends to zero. In reality, inertial effects of flow through the porous wall will become more significant for low KC numbers, so that the added mass will tend to some small positive value rather than zero. For larger KC numbers the damping also tends to zero, as the porous cylinder behaves more like a solid cylinder, for which the damping is zero in inviscid flow. Molin and Legras (1990) added a viscous force of the form $F_d = \rho C_d a d |U| U$ to the force from the potential model, to correct for neglecting viscous effects away from the porous wall. They found that this gave good agreement with experimental measurements of damping forces on porous cylinders.

To illustrate the relative magnitude of the damping on porous and solid cylinders, we can re-write (38) as

$$\frac{b_{11}^{drag}}{\omega \rho \pi a^2 d} = \frac{8}{3\pi^3} C_d KC. \tag{58}$$

Approximating C_d using (40) gives

$$\frac{b_{11}^{drag}}{\omega \rho \pi a^2 d} \approx 2.26 \beta^{-1/2} + 0.0172 KC^2, \quad \text{for } KC < 10. \tag{59}$$

The damping from (59) is shown in Fig. 15(d) for a value of $\beta = 1000$. The damping for the porous cylinders is significantly in excess of that for the solid cylinder for lower KC numbers. For higher KC numbers, the damping from the potential flow model tends to zero. It is expected that in reality, the damping would tend towards that for the solid cylinder at higher KC. However, Durhasan et al. (2019) found that the drag coefficient of a solid cylinder with a porous shroud in steady flow was slightly below that for a solid cylinder of the same diameter as the porous shroud. We may therefore expect that the same may apply for a fully porous cylinder in oscillatory flow. To quantify the actual damping on a porous cylinder in oscillatory flow will require further experimental tests or numerical modelling which incorporates viscous effects.

6.2. Truncated cylinder with porous lower section

In this section we investigate the effect of incorporating a porous chamber into a vertical truncated cylinder. The cylinder has draft d and radius a and is floating in infinite water depth. The lower section of the cylinder is porous, with the height of the porous section equal to d_p and height of solid section equal to $d_s = d - d_p$. A sketch of the geometry is shown in Fig. 16. To simplify the analysis and avoid making assumptions about the mass and mooring properties of the structure, we consider the diffraction and radiation cases only, rather than the case of body motions in waves.
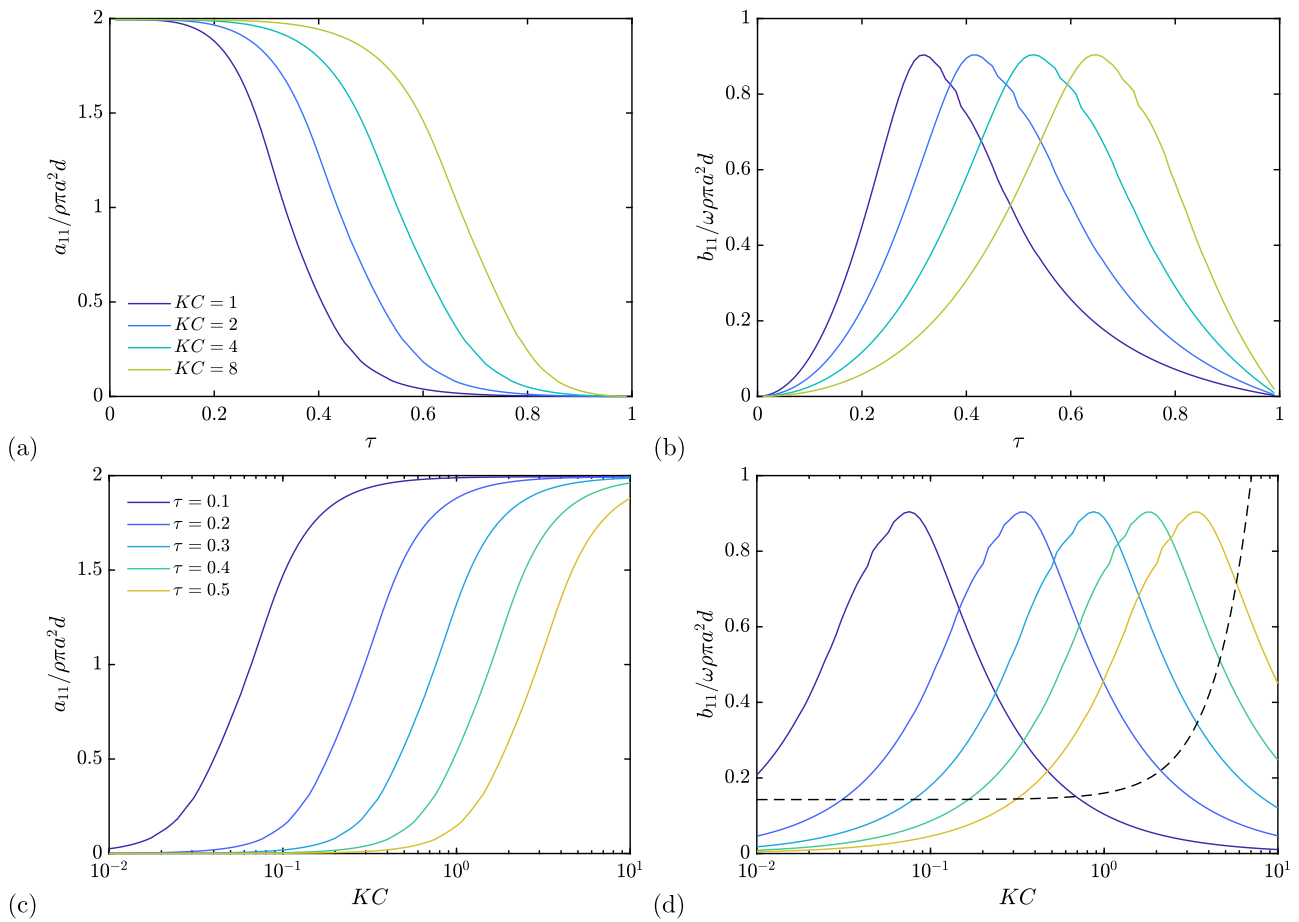
Fig. 15. Non-dimensional surge added mass and damping coefficients for a 2D porous cylinder in oscillatory flow plotted against porosity for various porosities (upper plots) and against KC number for various porosities (lower plots). Dashed line corresponds to viscous drag damping for a solid cylinder, calculated using (59) with $\beta = 1000$.
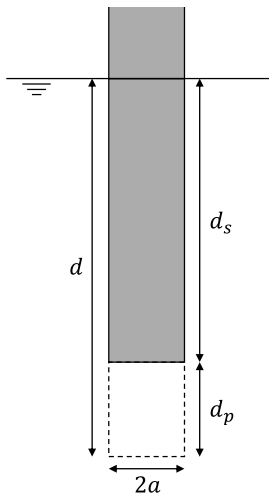

Fig. 16. Dimensions of truncated cylinder with porous lower section.

In the current example we consider a draft to radius ratio of $d/a = 10$ and a porous section of length ratio $d_p = d/4$. The wave amplitude is set at $A = a$. Pitch motions are assumed to be about the mean free surface in the centre of the cylinder and the motion amplitudes are fixed at $\xi_1 = a$ and $\xi_5 = a\sin(a/d)$, so that the displacement of the bottom of the structure in the pitch mode is equal to ξ_1.

Fig. 17 shows the surge and pitch excitation forces for various porosities. The surge excitation force shows very little change from the addition of the lower section, with a slight increase at low frequencies when the lower section is solid. The lower chamber has more influence on the pitch excitation force, with the solid lower cylinder giving around 30% higher peak excitation force. As before, the excitation forces for the porous cylinders are between the cases with $\tau = 0$ and $\tau = 1$.

The added mass and inertia are shown in Fig. 18. The mass and moment of inertia of the entrained mass of water in the lower chamber has been added to the values for the case with $\tau = 0$. The lower chamber significantly increases the added mass in both the surge and pitch modes. Adding a solid lower chamber would have the effect of lowering the natural frequency of the response compared to the case with no lower chamber. Increasing the porosity of the lower chamber reduces the added mass and would increase the natural frequency towards the case with no lower chamber.

Fig. 19 shows the normalised surge and pitch damping and the contributions from wave radiation and porous dissipation. For surge, the peak radiation damping is approximately equal to the maximum porous damping. However, the porous damping coefficient is approximately constant with frequency, as for the case of the 2D porous cylinder. In the present 3D case, the porous damping per unit length of the porous section is slightly higher than in the 2D case, since the porous damping here also includes a component due to flow through the bottom of the porous section.

In contrast, the radiation damping in pitch is an order of magnitude smaller than the porous damping. For comparison, the normalised pitch viscous damping coefficient for a solid lower cylinder can be calculated
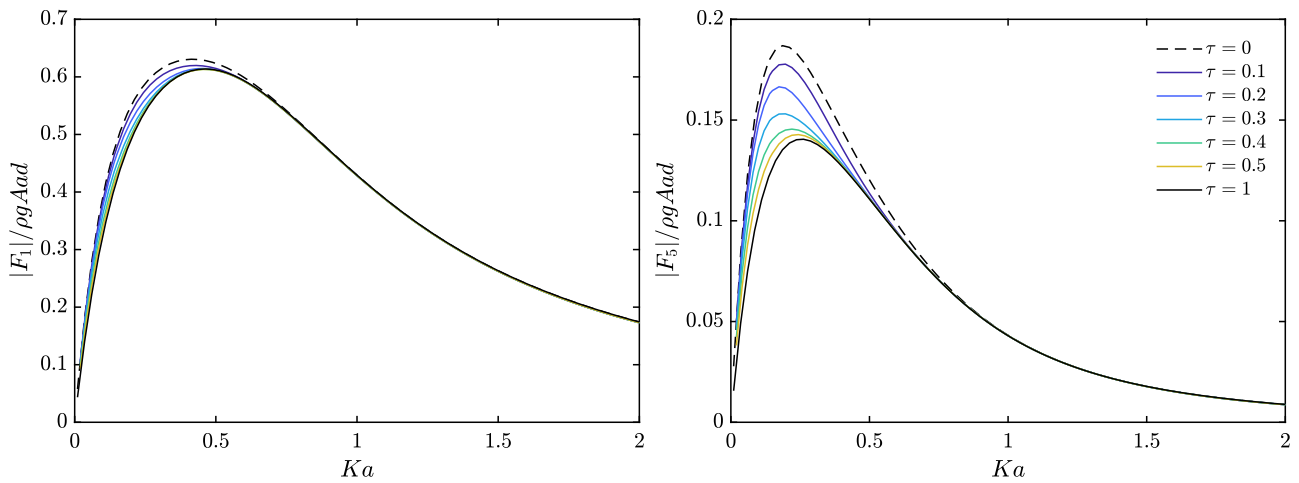
Fig. 17. Non-dimensional surge and pitch excitation forces on the truncated porous cylinder with dimensions $d/a = 10$, $d_p = d/4$ and wave amplitude $A = a$.
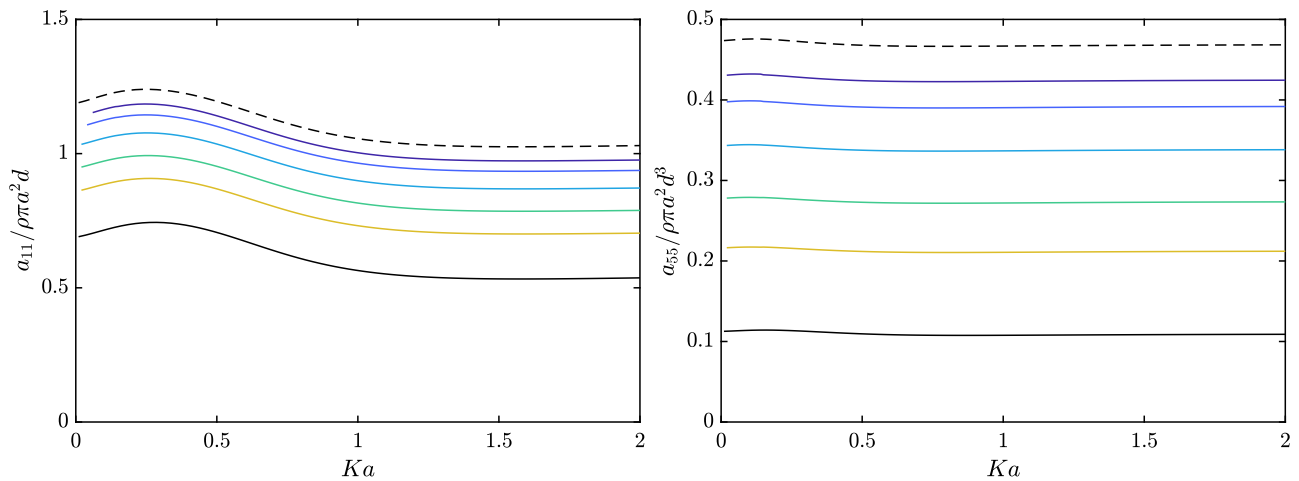

Fig. 18. Non-dimensional surge added mass and pitch added inertia for the truncated porous cylinder with dimensions $d/a = 10$, $d_p = d/4$ for motion amplitudes $\xi_1 = a$ and $\xi_5 = \sin^{-1}(a/d)$. See Fig. 17 for legend.

by integrating the viscous drag force over the length of the lower section, to give

$$\frac{b_{55}^{drag}}{\rho\omega\pi a^2 d^3} = \frac{2}{3\pi^2} C_d \xi_5 \frac{d^4 - d_s^4}{ad^3}, \tag{60}$$

where, for simplicity, it has been assumed that the drag coefficient is constant over the length of the lower section. For the present case, where $KC = \pi$ at the bottom of the structure, we have $C_d \approx 1$ and the normalised pitch viscous damping coefficient is

$$\frac{b_{55}^{drag}}{\rho\omega\pi a^2 d^3} \approx 0.05. \tag{61}$$

The normalised pitch porous damping coefficients shown in Fig. 19 are in the range 0.05–0.15, with porosities of $0.3 \leq \tau \leq 0.5$ all leading to similar damping levels around 0.15. So in this case, using a porous lower section could lead to higher damping than a lower solid section for small motion amplitudes. At higher motion amplitudes the viscous damping for the solid cylinder will increase and the porous damping will decrease. However, given the limitations of the current numerical approach discussed above, further studies will be required to quantify the damping for the porous cylinders.

7. Conclusions

The comparisons with experimental measurements have shown that the BEM model with a quadratic pressure drop across the porous surface is able to accurately predict the excitation forces on fixed porous cylinders both with and without a solid inner cylinder. The model is able to capture the nonlinear variation of the force with the wave amplitude. It was also demonstrated that the BEM model gives good qualitative agreement with the motion response of the TLP model with various porous outer cylinders.

The numerical investigations for the 2D porous cylinder indicated that for low KC numbers the dissipation across the porous surface leads to significantly higher damping than the viscous damping for a solid cylinder. The increased damping provided by the porous cylinder leads to a lower motion response for the TLP model. The numerical method used in the present study does not account for viscous effects away from the porous wall, so further studies are required to quantify the damping at higher KC numbers. However, the current numerical and experimental results indicate that for floating structures, including porous elements lower in the water column could be beneficial for reducing motion responses.

The numerical and experimental results showed that adding a porous outer cylinder to a solid vertical cylinder leads to increased excitation forces. Further investigation is needed to determine the load characteristics if the porous section was directly integrated in the pile
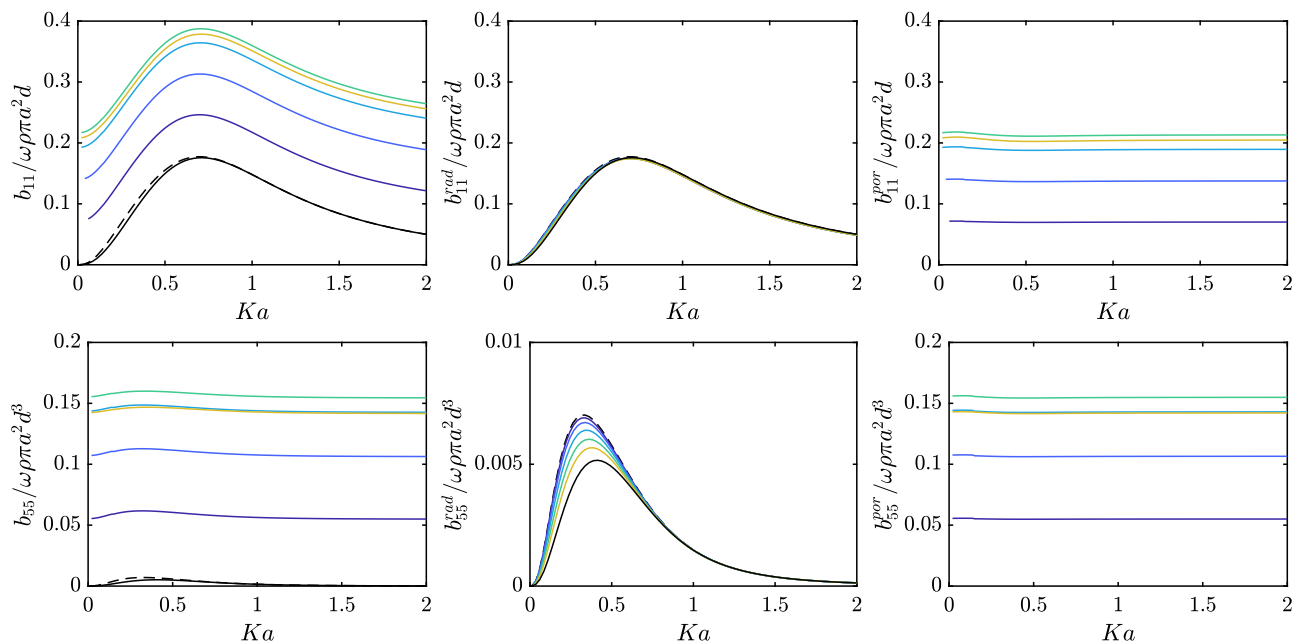
Fig. 19. Non-dimensional surge and pitch damping for the truncated porous cylinder with dimensions $d/a = 10$, $d_p = d/4$ for motion amplitudes $\xi_1 = a$ and $\xi_5 = \sin^{-1}(a/d)$. See Fig. 17 for legend.

structure, without increasing the physical dimensions. Structural and engineering considerations to achieve suitable solutions need to be assessed.

CRediT authorship contribution statement

Ed Mackay: Conceptualization, Methodology, Software, Investigation, Formal analysis, Writing – original draft. **Wei Shi:** Investigation, Writing – review & editing. **Dongsheng Qiao:** Investigation. **Roman Gabl:** Investigation, Writing – review & editing. **Thomas Davey:** Investigation, Writing – review & editing. **Dezhi Ning:** Funding acquisition, Writing – review & editing. **Lars Johanning:** Funding acquisition, Writing – review & editing.

Declaration of competing interest

The authors declare that they have no known competing financial interests or personal relationships that could have appeared to influence the work reported in this paper.

Acknowledgements

References

An, S., Faltinsen, O.M., 2012. Linear free-surface effects on a horizontally submerged and perforated 2D thin plate in finite and infinite water depths. Appl. Ocean Res. 37 (7491), 220–234. http://dx.doi.org/10.1016/j.apor.2012.04.006.

An, S., Faltinsen, O.M., 2013. An experimental and numerical study of heave added mass and damping of horizontally submerged and perforated rectangular plates. J. Fluids Struct. 39, 87–101. http://dx.doi.org/10.1016/j.jfluidstructs.2013.03.004.

Bearman, P.W., Downie, M.J., Graham, J.M.R., Obasaju, E.D., 1985. Force on a circular cylinder in viscous oscillatory flow at low Keulegan–Carpenter numbers. J. Fluid Mech. 154, 337–356.

Bearman, P.W., Russell, M., 1996. Measurements of hydrodynamic damping of bluff bodies with application to the prediction of viscous damping of TLP hulls. In: 21st Symposium On Naval Hydrodynamics, Trondheim, Norway, pp. 61–73.

Bennett, G.S., McIver, P., Smallman, J.V., 1992. A mathematical model of a slotted wavescreen breakwater. Coast. Eng. 18 (3–4), 231–249. http://dx.doi.org/10.1016/0378-3839(92)90021-L.

Chwang, A.T., 1983. A porous wavemaker theory. J. Fluid Mech. 132, 395–406.

Crowley, S., Porter, R., 2012. An analysis of screen arrangements for a tuned liquid damper. J. Fluids Struct. 34, 291–309. http://dx.doi.org/10.1016/j.jfluidstructs.2012.06.001.

Dai, J., Wang, C.M., Utsunomiya, T., Duan, W., 2018. Review of recent research and developments on floating breakwaters. Ocean Eng. 158, 132–151.

Darwiche, M., Williams, A., Wang, K., 1994. Wave interaction with a semi-porous cylindrical breakwater. J. Waterway Port Coastal Ocean Eng. 120 (4), 382–403.

Dokken, J., Grue, J., Karstensen, L.P., 2017a. Wave analysis of porous geometry with linear resistance law. J. Mar. Sci. Appl. 16 (4), 480–489. http://dx.doi.org/10.1007/s11804-017-1438-2.

Dokken, J.S., Grue, J., Karstensen, L.P., 2017b. Wave forces on porous geometries with linear and quadratic pressure-velocity relations. In: 32nd International Workshop on Water Waves and Floating Bodies, Dalian, China.

Downie, M.J., Graham, J.M., Hall, C., Incecik, A., Nygaard, I., 2000a. An experimental investigation of motion control devices for truss spars. Mar. Struct. 13, 75–90.

Downie, M., Wang, J., Graham, J., 2000b. The Effectiveness of Porous Damping Devices. In: 10th International Offshore and Polar Engineering Conference, pp. 418–425.

Durhasan, T., Pinar, E., Ozkan, G.M., Akilli, H., Sahin, B., 2019. The effect of shroud on vortex shedding mechanism of cylinder. Appl. Ocean Res. 84 (2018), 51–61. http://dx.doi.org/10.1016/j.apor.2019.01.007.

Evans, D.V., 1990. The use of porous screens as wave dampers in narrow wave tanks. J. Eng. Math. 24 (3), 203–212. http://dx.doi.org/10.1007/BF00058466.

Faltinsen, O.M., Firoozkoohi, R., Timokha, A.N., 2011. Steady-state liquid sloshing in a rectangular tank with a slat-type screen in the middle: Quasilinear modal analysis and experiments. Phys. Fluids 23 (4), http://dx.doi.org/10.1063/1.3562310.

Fugazza, M., Natale, L., 1992. Hydraulic design of perforated breakwaters. J. Waterw. Port Coast. Ocean Eng. 118 (1), 1–14. http://dx.doi.org/10.1061/(asce)0733-950x(1992)118:1(1).

Goupee, A.J., Koo, B.J., Kimball, R.W., Lambrakos, K.F., Dagher, H.J., 2014. Experimental comparison of three floating wind turbine concepts. J. Offshore Mech. Arct. Eng. 136, 1–9.

Graham, J.M., 1980. The forces on sharp-edged cylinders in oscillatory flow at low Keulegan–Carpenter numbers. J. Fluid Mech. 97 (2), 331–346. http://dx.doi.org/10.1017/S0022112080002595.

Huang, Z., Li, Y., Liu, Y., 2011. Hydraulic performance and wave loadings of perforated / slotted coastal structures : A review. Ocean Eng. 38 (10), 1031–1053.

Jonkman, J., Butterfield, S., Musial, W., Scott, G., 2009. Definition of a 5-MW Reference Wind Turbine for Offshore System Development. Tech. Rep., National Renewable Energy Laboratory.

Kim, B., 1998. Interactions of Waves, Seabed and Structures (Ph.D. dissertation). Seoul National University.

Koo, B., Goupee, A.J., Lambrakos, K., Kimball, R.W., 2012. Model tests for a floating windturbine on three different floaters. In: 31st International Conference on Offshore Mechanics and Arctic Engineering, Vol. 7, pp. OMAE2012-83642.

Kriebel, D.L., 1992. Vertical wave barriers: Wave transmission and wave forces. In: 23rd International Conference on Coastal Engineering. pp. 1313–1326. http://dx.doi.org/10.1061/9780872629332.099.

Li, Y., Liu, Y., Teng, B., 2006. Porous effect parameter of thin permeable plates. Coastal Eng. J. 48 (4), 309–336. http://dx.doi.org/10.1142/S0578563406001441.

Li, Y., Sun, L., Teng, B., 2004. Wave interaction with an array of combined cylinders with solid interior column and porous exterior column. In: 6th ISOPE Pacific/Asia Offshore Mechanics Symposium. International Society of Offshore and Polar Engineers.

Liu, Y., Li, Y.C., 2016. Predictive formulas in terms of Keulegan–Carpenter numbers for the resistance coefficients of perforated walls in Jarlan-type caissons. Ocean Eng. 114, 101–114. http://dx.doi.org/10.1016/j.oceaneng.2016.01.007.

Liu, Y., Li, H.J., 2017. Iterative multi-domain BEM solution for water wave reflection by perforated caisson breakwaters. Eng. Anal. Bound. Elem. 77 (238), 70–80. http://dx.doi.org/10.1016/j.enganabound.2016.12.011.

Liu, J., Lin, G., Li, J., 2012. Short-crested waves interaction with a concentric cylindrical structure with double-layered perforated walls. Ocean Eng. 40, 76–90. http://dx.doi.org/10.1016/j.oceaneng.2011.12.011.

Love, J.S., Tait, M.J., 2010. Nonlinear simulation of a tuned liquid damper with damping screens using a modal expansion technique. J. Fluids Struct. 26 (7–8), 1058–1077. http://dx.doi.org/10.1016/j.jfluidstructs.2010.07.004.

MacCamy, C., Fuchs, R., 1954. Wave Forces on Piles: A Diffraction Theory, Beach Erosion Board, Tech. Memo 69.

Mackay, E., Feichtner, A., Smith, R.E., Thies, P.R., Johanning, L., 2018. Verification of a boundary element model for wave forces on structures with porous elements. In: 3rd International Conference on Renewable Energies Offshore, RENEW 2018, pp. 341–350.

Mackay, E., Johanning, L., 2020. Comparison of analytical and numerical solutions for wave interaction with a vertical porous barrier. Ocean Eng. 199 (February), 107032. http://dx.doi.org/10.1016/j.oceaneng.2020.107032.

Mackay, E., Johanning, L., Ning, D., Qiao, D., 2019. Numerical and experimental modelling of wave loads on thin porous sheets. In: 38th International Conference on Ocean, Offshore and Arctic Engineering, pp. 1–10.

Mackay, E., Johanning, L., Shi, W., Ning, D., 2020. Model tests of a TLP floating offshore wind turbine with a porous outer column. In: International Society of Offshore and Polar Engineers, pp. ISOPE2020–TPC–0178.

Mackay, E., Liang, H., Johanning, L., 2021. A BEM model for wave forces on structures with thin porous elements. J. Fluids Struct. 102, 103246. http://dx.doi.org/10.1016/j.jfluidstructs.2021.103246.

Mansard, E.P.D., Funke, E.R., 1980. The measurement of incident and reflected spectra using a least squares method. In: 17th Coastal Engineering Conference, pp. 154–172.

McIver, P., 1998. The blockage coefficient for a rectangular duct containing a barrier with a circular aperture. Appl. Ocean Res. 20, 173–178.

Mei, C., Liu, P., Ippen, A., 1974. Quadratic loss and scattering of long waves. J. Waterway Harbour Coastal Eng. Div. 100, 217–239.

Molin, B., 1989. On the added mass and damping of porous or slotted cylinders. In: 4th International Workshop on Water Waves & Floating Bodies, Oystese, Norway, URL http://www.iwwwfb.org.

Molin, B., 1993. A potential flow model for the drag of shrouded cylinders. J. Fluids Struct. 7, 29–38.

Molin, B., 2001. On the added mass and damping of periodic arrays of fully or partially porous disks. J. Fluids Struct. 15, 275–290.

Molin, B., 2011. Hydrodynamic modeling of perforated structures. Appl. Ocean Res. 33 (1), 1–11.

Molin, B., Fourest, J.-M., 1992. Numerical modeling of progressive wave absorbers. In: 7th INternational Workshop Water Waves & Floating Bodies.

Molin, B., Legras, J.-L., 1990. Hydrodynamic modeling of the Roseau tower stabilizer. In: 9th OMAE Conference, pp. 329–336.

Molin, B., Remy, F., 2013. Experimental and numerical study of the sloshing motion in a rectangular tank with a perforated screen. J. Fluids Struct. 43, 463–480. http://dx.doi.org/10.1016/j.jfluidstructs.2013.10.001.

Molin, B., Remy, F., 2015. Inertia effects in TLD sloshing with perforated screens. J. Fluids Struct. 59, 165–177. http://dx.doi.org/10.1016/j.jfluidstructs.2015.09.004.

Molin, B., Remy, F., Ripol, T., 2007. Experimental study of the heave added mass and damping of solid and perforated disks close to the free surface. In: International Congress of International Maritime Association of the Mediterranean, Varna, Bulgaria.

Ning, D.Z., Zhao, X.L., Teng, B., Johanning, L., 2017. Wave diffraction from a truncated cylinder with an upper porous sidewall and an inner column. Ocean Eng. 130 (2016), 471–481. http://dx.doi.org/10.1016/j.oceaneng.2016.11.043.

Ouled Housseine, C., de Hauteclocque, G., Malencia, S., Chen, X.-b., 2018. Hydro-dynamic Interactions of the Truncated Porous Vertical Circular Cylinder with Water Waves. In: 37th International Conference on Ocean, Offshore and Arctic Engineering, Madrid, Spain, pp. OMAE2018–78221.

Park, M.-S., Koo, W., Choi, Y., 2010. Hydrodynamic interaction with an array of porous circular cylinders. Int. J. Naval Archit. Ocean Eng. 2 (3), 146–154. http://dx.doi.org/10.2478/ijnaoe-2013-0031.

Qiao, D., Mackay, E., Yan, J., Feng, C., Li, B., Feichtner, A., Ning, D., Johanning, L., 2021. Numerical simulation with a macroscopic CFD method and experimental analysis of wave interaction with fixed porous cylinder structures. Mar. Struct. 80, 103096. http://dx.doi.org/10.1016/j.marstruc.2021.103096.

Rashidi, S., Hayatdavoodi, M., Esfahani, J.A., 2016. Vortex shedding suppression and wake control: A review. Ocean Eng. 126, 57–80. http://dx.doi.org/10.1016/j.oceaneng.2016.08.031.

Sankarbabu, K., Sannasiraj, S.A., Sundar, V., 2007. Interaction of regular waves with a group of dual porous circular cylinders. Appl. Ocean Res. 29 (4), 180–190. http://dx.doi.org/10.1016/j.apor.2008.01.004.

Sarpkaya, T., 1986. Force on a circular cylinder in viscous oscillatory flow at low Keulegan–Carpenter numbers. J. Fluid Mech. 165, 61–71.

Sollitt, C., Cross, R., 1972. Wave transformation through permeable breakwaters. In: 13th International Conference on Coastal Engineering, pp. 1827–1846.

Song, H., Tao, L., 2007. Short-crested wave interaction with a concentric porous cylindrical structure. Appl. Ocean Res. 29 (4), 199–209. http://dx.doi.org/10.1016/j.apor.2008.01.001.

Stokes, G., 1851. On the effect of the internal friction of fluids on the motion of pendulums. Trans. Camb. Philos. Soc. 9, 8–106.

Suh, K.D., Kim, Y.W., Ji, C.H., 2011. An empirical formula for friction coefficient of a perforated wall with vertical slits. Coast. Eng. 58 (1), 85–93. http://dx.doi.org/10.1016/j.coastaleng.2010.08.006.

Sumer, B., Fredsoe, J., 2006. Hydrodynamics Around Cylindrical Structures, revised ed. vol. 26.

Tait, M.J., El Damatty, A.A., Isyumov, N., Siddique, M.R., 2005. Numerical flow models to simulate tuned liquid dampers (TLD) with slat screens. J. Fluids Struct. 20 (8), 1007–1023. http://dx.doi.org/10.1016/j.jfluidstructs.2005.04.004.

Tao, L., Dray, D., 2008. Hydrodynamic performance of solid and porous heave plates. Ocean Eng. 35 (10), 1006–1014.

Tao, L., Song, H., Chakrabarti, S., 2009. Scaled boundary FEM model for interaction of short-crested waves with a concentric porous cylindrical structure. J. Waterway Port Coastal Ocean Eng. 135 (5), 200–212. http://dx.doi.org/10.1061/(ASCE)0733-950X(2009)135:5(200).

Twu, S.W., Lin, D.T., 1991. On a highly effective wave absorber. Coast. Eng. 15 (4), 389–405. http://dx.doi.org/10.1016/0378-3839(91)90018-C.

Vijay, K.G., He, S.Y., Zhao, Y., Liu, Y., Sahoo, T., 2020a. Gravity wave interaction with a submerged wavy porous plate. Ships Offshore Struct. 1–11. http://dx.doi.org/10.1080/17445302.2020.1789034.

Vijay, K.G., Neelamani, S., Sahoo, T., 2019. Wave interaction with multiple slot-ted barriers inside harbour: Physical and numerical modelling. Ocean Eng. 193 (September), 106623. http://dx.doi.org/10.1016/j.oceaneng.2019.106623.

Vijay, K.G., Nishad, C.S., Neelamani, S., Sahoo, T., 2020b. Gravity wave interaction with a wave attenuating system. Appl. Ocean Res. 101 (May), 102206. http://dx.doi.org/10.1016/j.apor.2020.102206.

Wang, C., 1968. On high-frequency oscillatory viscous flows. J. Fluid Mech. 32 (1), 55–68. http://dx.doi.org/10.1017/S0022112068000583.

Wang, K., Ren, X., 1994. Wave interaction with a concentric porous cylinder system. Ocean Eng. 21 (4), 343–360.

Warnitchai, P., Pinkaew, T., 1997. Modelling of liquid sloshing in rectangular tanks with flow-dampening devices. Eng. Struct. 20 (7), 593–600.

Weng, Y., Xu, X., Huang, H., 2016. Interaction of cnoidal waves with an array of vertical concentric porous cylinders. Appl. Ocean Res. 58, 21–36. http://dx.doi.org/10.1016/j.apor.2016.01.011.

Williams, A.N., Li, W., 1998. Wave interaction with a semi-porous cylindrical break-water mounted on a storage tank. Ocean Eng. 25 (2–3), 195–219. http://dx.doi.org/10.1016/s0029-8018(97)00006-1.

Williams, A.N., Li, W., 2000. Water wave interaction with an array of bottom-mounted surface-piercing porous cylinders. Ocean Eng. 27 (8), 841–866. http://dx.doi.org/10.1016/S0029-8018(99)00004-9.

Williams, A.N., Li, W., Wang, K.H., 2000. Water wave interaction with a floating porous cylinder. Ocean Eng. 27, 1–28.

Yu, X., 1995. Diffraction of water waves by porous breakwaters. J. Waterway Port Coastal Ocean Eng. 121 (6), 275–282.

Zhao, F., Bao, W., Kinoshita, T., Itakura, H., 2010a. Interaction of waves and a porous cylinder with an inner horizontal porous plate. Appl. Ocean Res. 32 (2), 252–259. http://dx.doi.org/10.1016/j.apor.2009.11.003.

Zhao, F., Bao, W., Kinoshita, T., Itakura, H., 2010b. Theoretical and experimental study on a porous cylinder floating in waves. J. Offshore Mech. Arct. Eng. 133 (1), 011301. http://dx.doi.org/10.1115/1.4001435.